

AD-A174 370

CONFORMAL MICROSTRIP SLOT ANTENNA AND ANTENNA ARRAY(U)
MOORE SCHOOL OF ELECTRICAL ENGINEERING PHILADELPHIA PA
VALLEY M KISLIUK ET AL SEP 86 RADC-TR-86-0114

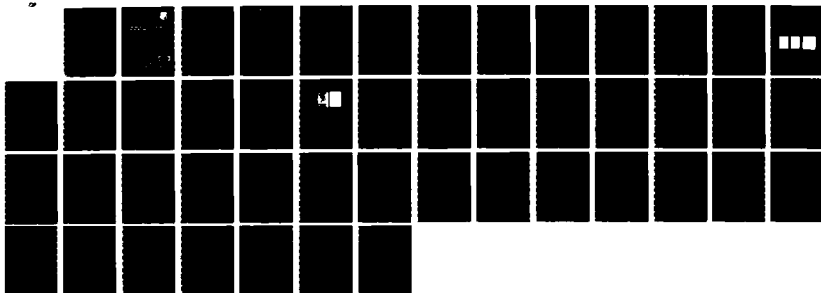
1/1

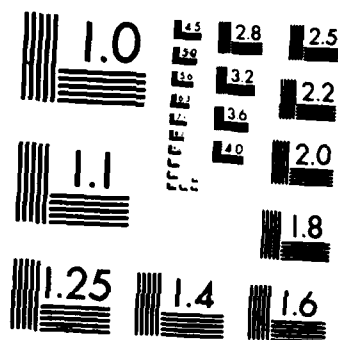
UNCLASSIFIED

F19628-84-K-0021

F/G 9/5

NL





MICROCOPY RESOLUTION TEST CHART
NATIONAL BUREAU OF STANDARDS-1963-A

12

RADC-TR-86-114
Interim Report
September 1986



CONFORMAL MICROSTRIP SLOT ANTENNA AND ANTENNA ARRAY

University of Pennsylvania

Moshe Kisliuk, Bernard Steinberg and William Whistler

AD-A174 370

APPROVED FOR PUBLIC RELEASE; DISTRIBUTION UNLIMITED

NTIC FILE COPY

DTIC
ELECTE
NOV 25 1986
S D
E

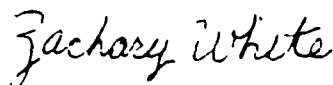
ROME AIR DEVELOPMENT CENTER
Air Force Systems Command
Griffiss Air Force Base, NY 13441-5700

46 1 25 032

This report has been reviewed by the RADC Public Affairs Office (PA) and is releasable to the National Technical Information Service (NTIS). At NTIS it will be releasable to the general public, including foreign nations.

RADC-TR-86-114 has been reviewed and is approved for publication.

APPROVED:



ZACHARY WHITE
Project Engineer

APPROVED:



ALLAN C. SCHELL
Chief, Electromagnetic Sciences Directorate

FOR THE COMMANDER:



JOHN A. RITZ
Plans and Programs Directorate

If your address has changed or if you wish to be removed from the RADC mailing list, or if the addressee is no longer employed by your organization, please notify RADC (EEAA) Hanscom AFB MA 01731-5000. This will assist us in maintaining a current mailing list.

Do not return copies of this report unless contractual obligations or notices on a specific document requires that it be returned.

UNCLASSIFIED

SECURITY CLASSIFICATION OF THIS PAGE

REPORT DOCUMENTATION PAGE

1a. REPORT SECURITY CLASSIFICATION UNCLASSIFIED			1b. RESTRICTIVE MARKINGS N/A		
2a. SECURITY CLASSIFICATION AUTHORITY N/A			3. DISTRIBUTION/AVAILABILITY OF REPORT Approved for public release; distribution unlimited		
2b. DECLASSIFICATION/DOWNGRADING SCHEDULE N/A					
4. PERFORMING ORGANIZATION REPORT NUMBER(S) N/A			5. MONITORING ORGANIZATION REPORT NUMBER(S) RADC-TR-86-114		
6a. NAME OF PERFORMING ORGANIZATION University of Pennsylvania		6b. OFFICE SYMBOL (If applicable)	7a. NAME OF MONITORING ORGANIZATION Rome Air Development Center (EEAA)		
6c. ADDRESS (City, State, and ZIP Code) Valley Forge Research Center Moore School of Electrical Engineering Philadelphia PA 19104			7b. ADDRESS (City, State, and ZIP Code) Hanscom AFB MA 01731-5000		
8a. NAME OF FUNDING / SPONSORING ORGANIZATION Rome Air Development Center		8b. OFFICE SYMBOL (If applicable) EEAA	9. PROCUREMENT INSTRUMENT IDENTIFICATION NUMBER F19628-84-K-0021		
8c. ADDRESS (City, State, and ZIP Code) Hanscom AFB MA 01731-5000			10. SOURCE OF FUNDING NUMBERS		
			PROGRAM ELEMENT NO 61102F	PROJECT NO 2305	TASK NO J3
			WORK UNIT ACCESSION NO 47		
11. TITLE (Include Security Classification) CONFORMAL MICROSTRIP SLOT ANTENNA AND ANTENNA ARRAY					
12. PERSONAL AUTHOR(S) Moshe Kisliuk, Bernard Steinberg, William Whistler					
13a. TYPE OF REPORT Interim		13b. TIME COVERED FROM Mar 85 TO Feb 86		14. DATE OF REPORT (Year, Month, Day) September 1986	
15. PAGE COUNT 52					
16. SUPPLEMENTARY NOTATION N/A					
17. COSATI CODES			18. SUBJECT TERMS (Continue on reverse if necessary and identify by block number)		
FIELD	GROUP	SUB-GROUP			
09	03		Microslot Antennae AWACS Airborne Arrays		
17	09		Conformal Antennae Radio Camera Airborne Sensors		
			Conformal Arrays Beamforming		
19. ABSTRACT (Continue on reverse if necessary and identify by block number)					
<p>This study explores the wideband potential of a microstrip-fed slot radiator as an element of a planar or conformal antenna array. The microstrip slot is seen to have 40% input impedance bandwidth under 1.5 VSWR and a demonstrated 10% gain bandwidth to 3db.</p> <p>The report describes an analytic slot model and experimental tests. A conclusion of this report is that useful high efficiency radiators (greater than 80%) can be made by using the microstrip slot in N-element serial arrays.</p>					
20. DISTRIBUTION/AVAILABILITY OF ABSTRACT <input type="checkbox"/> UNCLASSIFIED/UNLIMITED <input checked="" type="checkbox"/> SAME AS RPT <input type="checkbox"/> DTIC USERS			21. ABSTRACT SECURITY CLASSIFICATION UNCLASSIFIED		
22a. NAME OF RESPONSIBLE INDIVIDUAL Zachary White			22b. TELEPHONE (Include Area Code) (617) 861-2055		22c. OFFICE SYMBOL RADC (EEAA)

TABLE OF CONTENTS

Preface	
Summary	
Related Publications	
and Presentations.....	1
1. High Efficiency Microslot Study...	2.
1.1. Determination of	
Matching Technique.....	2
1.2. Effect of Feeding System	
on Antenna Patterns.....	4
1.3. Effects of Slot Area	
on Antenna Gain.....	6
1.4. Comparison of Shunt Microstrip	
Slot and Microstrip Patch	
Radiators.....	9
2. Series Slot Investigation.....	10
2.1. Match Improvement Techniques...	11
2.2. Dielectric Layer Truncation	
Effects.....	13
2.3. Series Slot Pattern.....	16
2.4. Gain and Efficiency.....	21
3. Radiation of Microstrip	
Meander-Line Slot Antenna.....	22
3.1. Fields in a Spherical	
Coordinate System.....	23
3.2. Radiation from the Slot.....	26
3.3. Radiation from Spillover	
Currents.....	29
3.4. Radiation from the Hybrid	
Surface Wave at the	
Truncations of the	
Dielectric.....	32
3.5. Tapered Meander Line Slot	
Array Investigations.....	35
4. Conclusions.....	38
References.....	40



Accession For	
NTIS GRA&I	<input checked="" type="checkbox"/>
DTIC TAB	<input type="checkbox"/>
Unannounced	<input type="checkbox"/>
Justification	
By _____	
Distribution/ _____	
Availability Codes	
Dist	Avail and/or Special
A-1	

RELATED PUBLICATIONS AND PRESENTATIONS

1. M. Kisliuk, "The Conformal Microstrip Slot Antenna," 1983 IEEE Int. Symp. Antennas and Prop., Vol. 1, Houston, TX, pp. 166-169.
2. M. Kisliuk, "The Voltage Distribution on Waveguide Fed Slot and Slit Antennas," IEEE Benjamin Franklin Symposium on Advances in Antennas and Microwave Technology Digest, Philadelphia, PA, 1983, pp. 13-15.
3. M. Kisliuk, "Lossy Transmission Line Model of Microstrip Slot Antenna," VFRC Quarterly Progress Report No. 43, April-September 1983, pp. 76-81.
4. M. Kisliuk, "Microstrip-fed Radiating Slots and Slot Arrays," VFRC Quarterly Progress Report No. 45, April-September 1984, pp. 46-48.
5. W. Whistler, "Microstrip Slot Antenna-Experimental Investigation, VFRC Quarterly Progress Report No. 45, April-September 1984.
6. M. Kisliuk, B.D. Steinberg and W. Whistler, "Conformal Microstrip Slot Antenna and Antenna Array," First Interim R & D Report, December 1985.
7. M. Kisliuk, A. Axelrod and Y. Servant, "Experimental Results on an H-Guide Slot Antenna with an 80% (and higher) Efficiency in a 21% Frequency Band," submitted in December 1985 for publication to Microwaves and RF.

LIST OF FIGURES

1.1	3-D Sketch of Microslot Shunt Radiator.....	3
1.2	Microslot Shunt Radiator: Pattern with Coaxial Edge-Board Feed.....	5
1.3	Microslot Shunt Radiator: Pattern with Coaxial Rear-Feed through Ground Plane.....	5
1.4	Photo of vee Slot, .5 mm and .2 mm Microslot Radiators used in Antenna Gain Studies.....	6
1.5	Pattern of .2 x 3.2 mm Microslot Antenna Measured at 9.154 GHz.....	7
1.6	Pattern of .5 x 10.9 mm Microslot Antenna Measured at 8.535 GHz.....	8
1.7	Pattern of a .5 mm Vee Slot Antenna shown in Figure 4 at 9.607 GHz.....	9
2.1	Front and Rear View of .2 x 12.6 mm Serial Microstrip Slot Test Board.....	12
2.2	Comparison of Single X-Band Slot VSWR Measure- ments at Tel-Aviv University and at VFRC.....	12
2.3	Antenna Pattern of .5 x 12.6 mm Microslot on 15.3 cm Dielectric Substrate.....	13
2.4	Antenna Pattern: Comparison of Patterns of .5 x 12.6 mm Slot Radiator with (Solid Line) and without 38 cm x 20 cm Ground Plane.....	15
2.5	VSWR pf .5 x 12.6 mm Slot Radiator used in Pattern Tests.....	17
2.6	Antenna Pattern: .5 x 12.6 mm Slot at 8.0 GHz.....	18
2.7	Antenna Pattern: .5 x 12.6 mm Slot at 9.0 GHz.....	18
2.8	Antenna Pattern: .5 x 12.6 mm Slot at 10.5 GHz.....	19
2.9	Antenna Pattern: .5 mm Vee Slot Antenna at 9.0 GHz..	19
2.10	Gain and Beam Tilt vs. Frequency Graphs for .5 x 12.6 mm and .2 x 14 mm Microstrip Slots and .5 mm Vee Slot Radiators.....	20
3.1	The Microstrip Meander-Line Slot Antenna.....	23
3.2	Spherical Coordinates in the Far-field Zone.....	24
3.3	Simplified Equivalent Circuit of a Microstrip Meander-Line Slot Antenna.....	28
3.4	13-Slot Array. The Width of Slots is Tapered.....	36
3.5	E-Plane Radiation Patterns of the Slot Array of Figure 3.4.....	37
3.6	10-Slot Array. The Width of the Microstrip Lines Feeding the Slot is Tapered.....	38
3.7	E-Plane Radiation Patterns of the Slot Array of Figure 3.6.....	38

PREFACE

The Valley Forge Research Center initiated this research to formulate theory and to develop microstrip antennae having radiating nonresonant slots in the upper conductor. Preliminary calculations indicated that such antennae can operate in a wider frequency band than the conventional patch microstrip antennae. Our original work to obtain high angular resolution microwave imaging led to the design of the Radio Camera. Implementation of the Radio Camera led to techniques for beamforming an array which is composed of randomly spaced elements, each element moving in a random fashion. The results of our experiments led us to believe that we could design a conformal microstrip slot antenna. The overall goal of this research effort is to develop an antenna element that may be flush-mounted in the outer skin of the aircraft and placed in an arbitrary location. These elements would be connected to a solid state RF located on the interior surface of the airframe by an electrical feedthrough.

SUMMARY

In the First Interim Report, a series of analytic developments were completed concerning the input impedance, pattern efficiency and losses of the microstrip slot antenna. Experimental verification was attempted at both Tel-Aviv University and VFRC with mixed results. One of the main implications for further research was the need to investigate improvements in antenna pattern measurement techniques. A section of this report is devoted to this topic.

The design of a high efficiency microstrip slot shunt radiator comparable to the microstrip patch antenna is a second area of investigation reported here. Capacity coupling to the microstrip slot as a resonator produced antenna gain and efficiencies that approaches, but did not exceed, the directivity of the patch radiator.

Other conclusions of the shunt radiator study were that increasing slot radiator area improved antenna gain and efficiency. In addition, the effects of metal plate edges and dielectric truncations were more easily studied on the higher efficiency shunt microstrip slot radiator.

Analytic investigations of microstrip slot characteristics continued in this report period. Emphasis was placed on hybrid surface waves, a non-radiating mode and radiation from a truncated dielectric edge.

1. HIGH EFFICIENCY MICROSLLOT STUDY

It is evident that a high efficiency slot would be more universally useful than the low efficiency slot, since the latter can only achieve useful efficiencies ($> 80\%$) by the formation of a series slot array. An antenna element with broad beam pattern in two orthogonal planes is more desirable for wide angle two dimensional arrays, so a study of methods of terminating a line with a microstrip slot was initiated.

A method of matching by capacity coupling has been found and is described. An antenna study has been conducted which shows the microstrip slot radiator exhibiting an increase in gain as the slot area is increased. Currents in the metal surrounding the slot excite nonradiating hybrid modes in the dielectric, which radiate at the edges of the dielectric. When compared to the microstrip patch radiator, the microslot radiator's pattern is broader and gain is lower. Its bandwidth in this mode appears lower than the patch radiator's for the same dielectric thickness.

1.1. DETERMINATION OF MATCHING TECHNIQUE

To begin the study, experiments were made to find a suitable matching network for a radiator terminating a 50 line microstrip line. A matching stub following the microslot was investigated and rejected, after trials of a series of stub lengths of various impedances produced no indication of

matching potential. Attempts at matching by varying the input line impedance to present different impedance levels to the microslot also produced only high input reflection conditions.

A successful matching system was finally obtained by capacity coupling to the transverse microstrip line containing the slot, treating this last as a resonant circuit. This system could always be made to match by adjusting capacity by varying coupling slot width. The resulting configuration is shown in Figure 1.1.

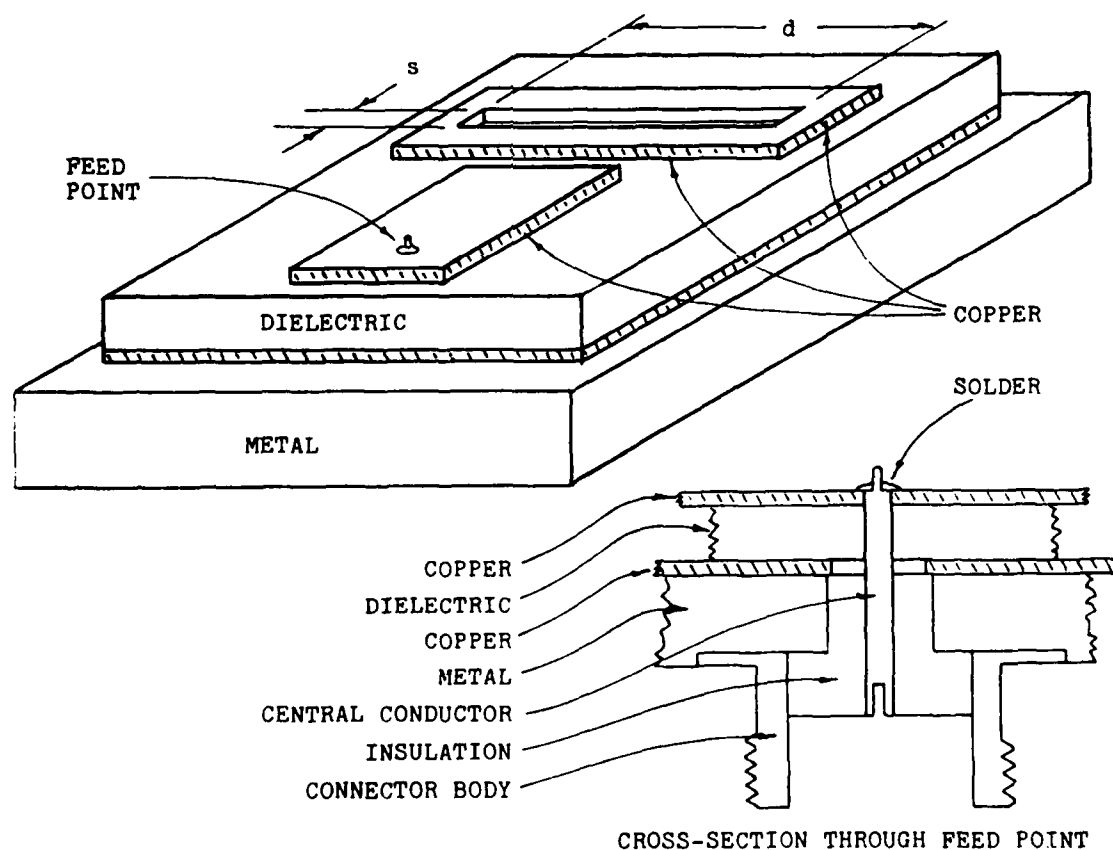


FIGURE 1.1. 3-D SKETCH OF MICROSLLOT SHUNT RADIATOR

A useful measurement parameter is the cavity Q of this resonant circuit. For any shunt resonant circuit, cavity resonance is indicated by zero reactance, or a normalized impedance of $1 + j0$. The reciprocal of the frequency difference between the ± 45 degree phase conditions or between normalized impedances of $1 \pm j1$ is defined as the cavity Q. VSWR at the level $1 \pm j1$ impedance levels is 2.6:1 : this level is similar to the 2:1 and 3:1 bandwidths common in discussing microstrip patches and other radiators, and is convenient for comparing this radiator with others.

Resonant frequency of the shunt microslot radiator is directly related to the total path length of the 100 ohm metal line surrounding the microstrip slot using the effective dielectric constant calculated for the 100 ohm line. Typical cavity Q's for the radiators measured here varied between .6% and .76% for a .031" (.787 mm) thick substrate. Resonant frequencies varied from 8 GHz to 9.6 GHz for various configurations; for a representative frequency of 9 GHz, this thickness is $.024 \lambda$.

1.2 EFFECT OF FEEDING SYSTEM ON ANTENNA PATTERNS

The First Interim Report noted in its conclusions the need for improving the feed system to reduce feed effects on pattern. The pattern in Figure 1.2 is typical of the edge feeding system. The beam peak of the shunt-fed microslot radiator shows a beam tilt of 48 degrees, indicating the influence of direct radiation from the coaxial feed at board edge.

The pattern improvement obtained by using the rear feed with entry point through the ground plane is clearly shown in Figure 3. This pattern shows a more uniform pattern with the beam tilt reduced to 15 degrees. The beam tilt remaining is believed to be caused by radiation from the coaxial feedline or the $.33 \lambda$ long 50 ohm microstrip feedline.

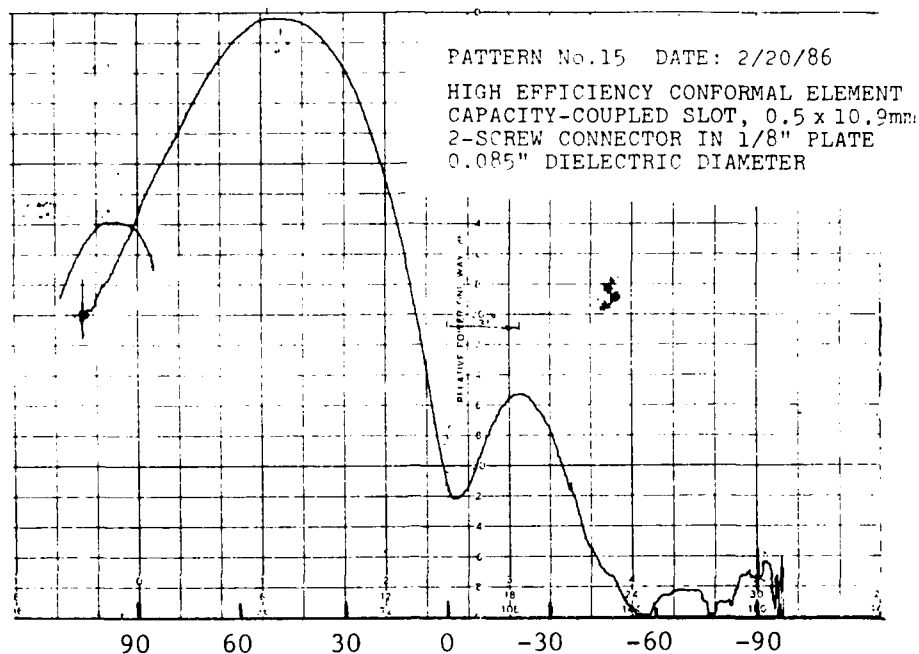


FIGURE 1.2 MICROSLLOT SHUNT RADIATOR: PATTERN WITH COAXIAL
 EDGE-BOARD FEED.

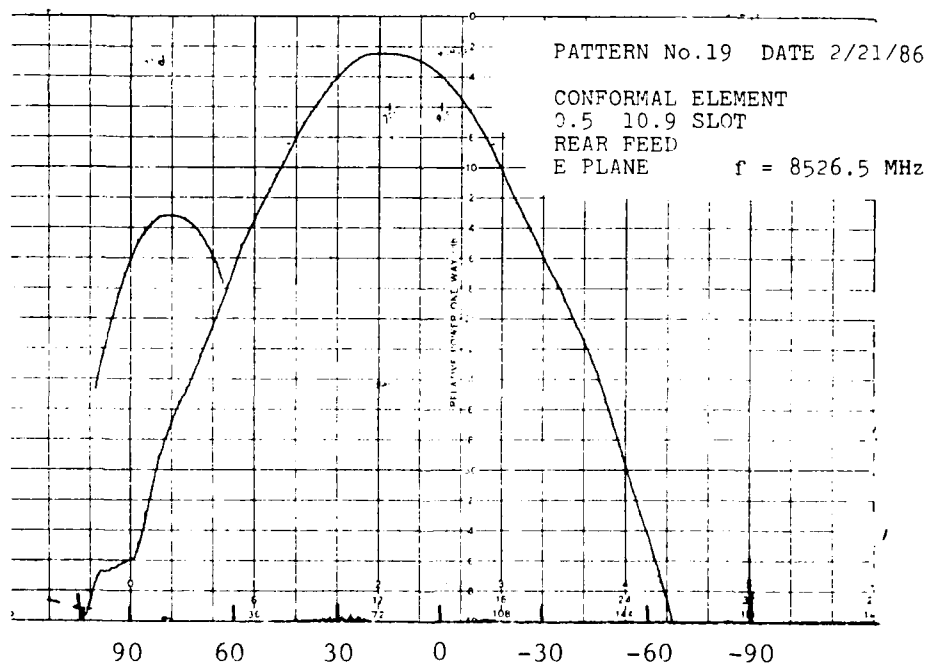


FIGURE 1.3. MICROSLLOT SHUNT RADIATOR: PATTERN WITH COAXIAL REAR-FEED
 THROUGH GROUND PLANE.

The rear feed approach has been adopted in all succeeding testing because of its clear reduction of interference from direct radiation with the microslot radiator patterns.

1.3 EFFECTS OF SLOT AREA ON ANTENNA GAIN

The microslot as a shunt radiator acts like a slot antenna in a ground plane with respect to antenna gain, having a low radiation efficiency because of low physical area. To investigate the effect of radiator area on gain, the three substrates shown in Figure 1.4 were fabricated.

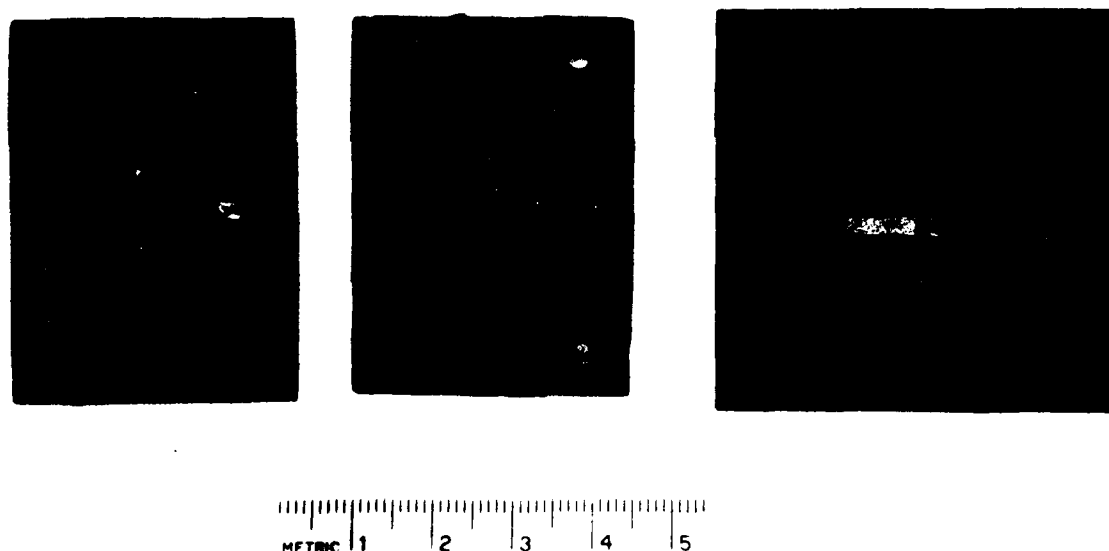


FIGURE 1.4. PHOTO OF VEE SLOT, .5 MM AND .2 M MICROSLLOT RADIATORS USED IN ANTENNA GAIN STUDIES.

The .2 mm microslot's antenna pattern is shown in Figure 1.5. The appearance of shoulders on the main lobe pattern is believed due to radiation

from the dielectric truncations at ± 1.78 cm from the center of the microslot (the substrate edges). They are most prominent in this low-gain microslot because they are similar in magnitude to the direct microslot radiation. The extraneous radiation at $+90$ degrees and at 180 degree angles cannot be caused by the microslot because its pattern factor approaches zero for end fire direction. End fire radiation thus must be caused by radiation of hybrid mode energy from the truncated dielectric edges of the substrate.

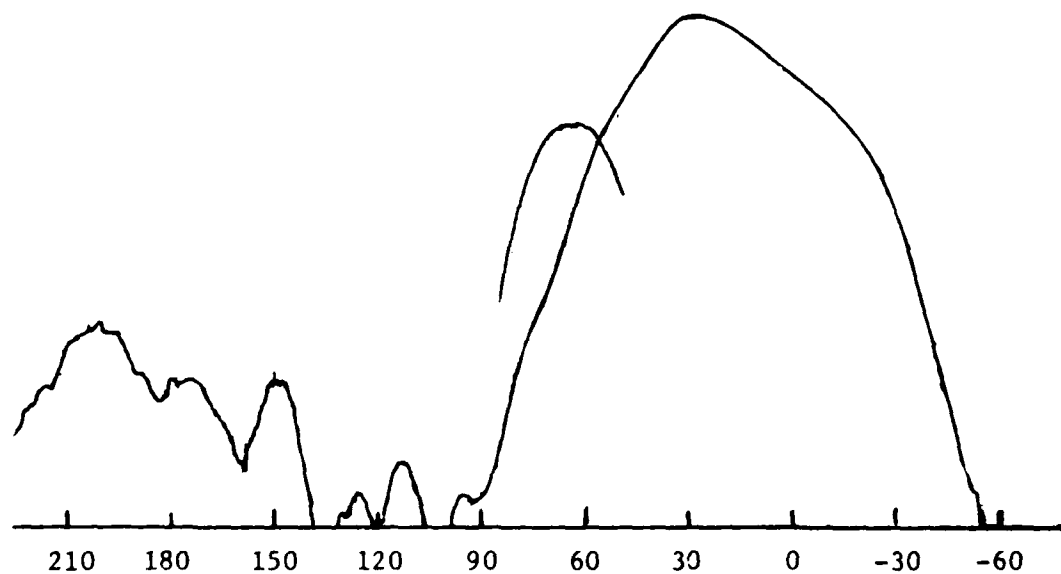


FIGURE 1.5. PATTERN OF .2 X 13.2 MM MICROSLLOT ANTENNA MEASURED AT 9.154 GHz. MEASURED GAIN IS - 1.5 dB BELOW THAT OF A DIPOLE RADIATOR (-1.5 DBD).

The .5 mm shunt microslot antenna pattern of Figure 1.6 shows considerable reduction of shoulders from dielectric edge radiation, probably because of the 2.3 dB increase in gain for this radiator.

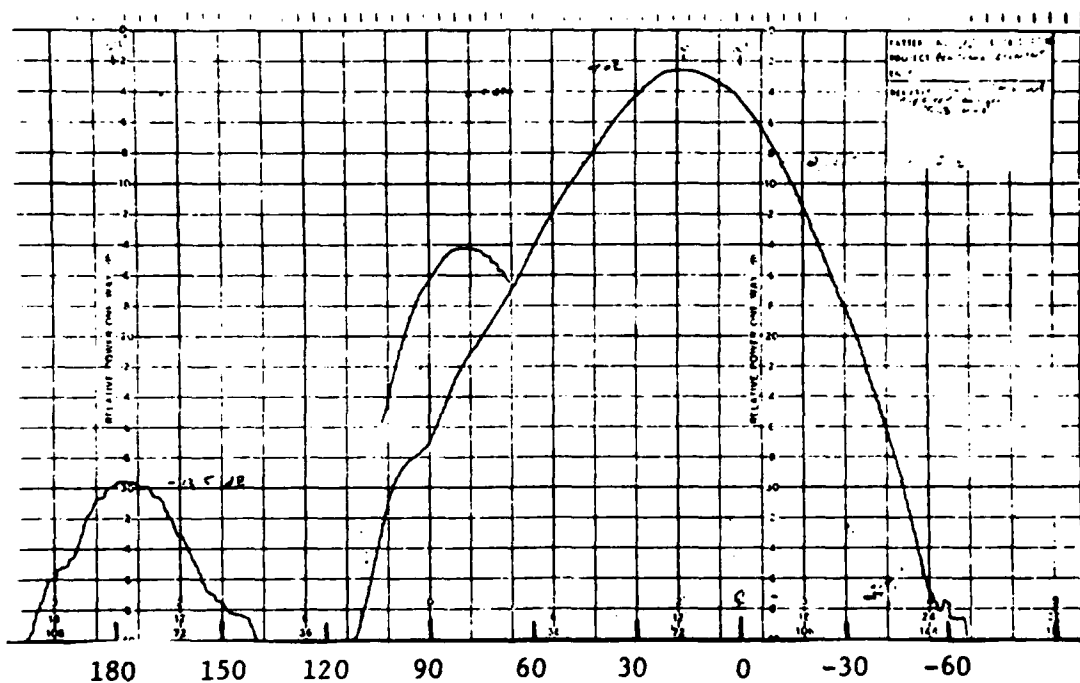


FIGURE 1.6. PATTERN OF .5 X 10.9 MM MICROSLLOT ANTENNA MEASURED AT 8.535 GHz. MEASURED ANTENNA GAIN IS + .8 dBd.

The gain increase with the wider slot prompted the design of the "vec-slot" radiator which was hand fabricated because of time pressures. The resulting pattern shown in Figure 1.7 exhibits a 4.2 dB gain increase over the .5 mm microslot pattern. This is a significant gain improvement and is the shunt microstrip slot radiator form most closely competitive with the microstrip patch radiator.

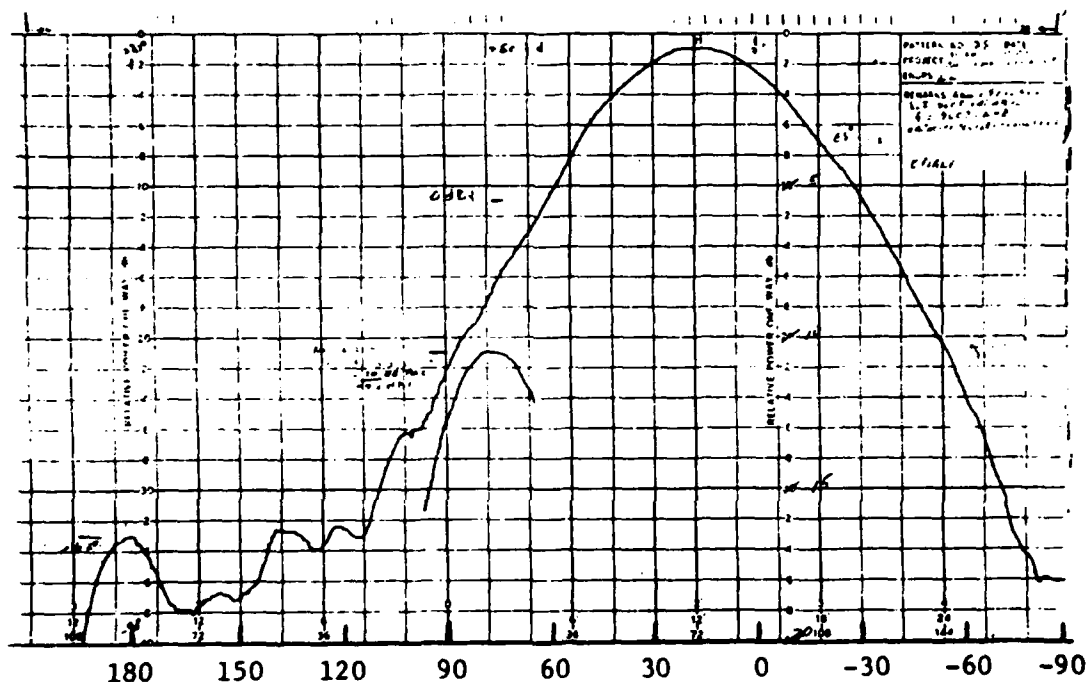


FIGURE 1.7. PATTERN OF .5 MM VEE SLOT ANTENNA SHOWN IN FIGURE 4 AT 9.607 GHz. MEASURED ANTENNA GAIN IS 5 dB.

1.4 COMPARISON OF SHUNT MICROSTRIP SLOT AND MICROSTRIP PATCH RADIATORS

A comparison of the microstrip vee-slot and patch radiators is given in Table 1.

TABLE 1. COMPARISON OF PATCH AND VEE SLOT RADIATORS
Vee-Slot Microslot Microstrip Patch*

Gain	+5 dBd measured	+6.7 dBd Calculated
Bandwidth	.64% measured	2.4% Calculated
2:1VSWR	for $t/\lambda_0 = .035$	for $t/\lambda_0 = .035$

*Source: Reference [11]

Most significant is that the vee-slot antenna measured gain approaches that of the calculated microstrip patch gain.

Bandwidth for $VSWR = 2:1$ indicates superior performance for the patch antenna. These are directions indicated for improving vee slot bandwidth, the principal one being to use a lower impedance line to surround the microstrip slot. However, it appears impossible for the vee slot bandwidth to approach the patch bandwidth.

The capacity coupling method used in feeding the vee slot is difficult to control tolerances on if edge coupling of microstrip lines is the capacity mechanism. Any other capacity mechanism, such as soldered-on chip capacitors, nullifies the microstrip advantage of being a low cost fabrication process.

To summarize, the vee slot antenna appears to be the microstrip slot implementation that is the closest competitor for the microstrip patch antenna. Its lower bandwidth and tolerance-sensitive coupling mechanism make it inferior to the patch for similar applications in its present form.

2. SERIES SLOT INVESTIGATION

The series microstrip slot as originally conceived by Prof. Kisliuk continues to be the main thrust of this contract's effort. Efforts were made in this report period to improve pattern measurement techniques and to broaden our understanding of the microstrip slot antenna.

A pattern study of a series slot radiator is detailed, with patterns taken in a test fixture that minimizes the pattern interference of the dielectric truncation radiation.

2.1 MATCH IMPROVEMENT TECHNIQUES

An impedance study of the rear-mounted connector was made using two rear-mounted connectors mounted on a 13.72 cm (5.4") 50 ohm line. The connector matching time cycle was shortened by the discovery that a tapered resistive card laid on top of the microstrip offered more than 10 dB insertion loss and thus isolated reflections from the distant connector from those of the input port connector by attenuation. This system allowed studying connector impedance by modifying only the input connector dimensions.

A connector having a .085" teflon diameter was chosen because the .093" wide 50 ohm line will block direct radiation from the feedline. The original .010" diameter center conductor introduced a fixed series inductance: this was minimized by increasing the center conductor diameter to .027".

The final connector configuration is shown in Figure 2.1. The resulting single connector VSWR was under 1.1 VSWR from 8.0 to 11.0 GHz. This design is duplicated in all test fixtures used in this report period.

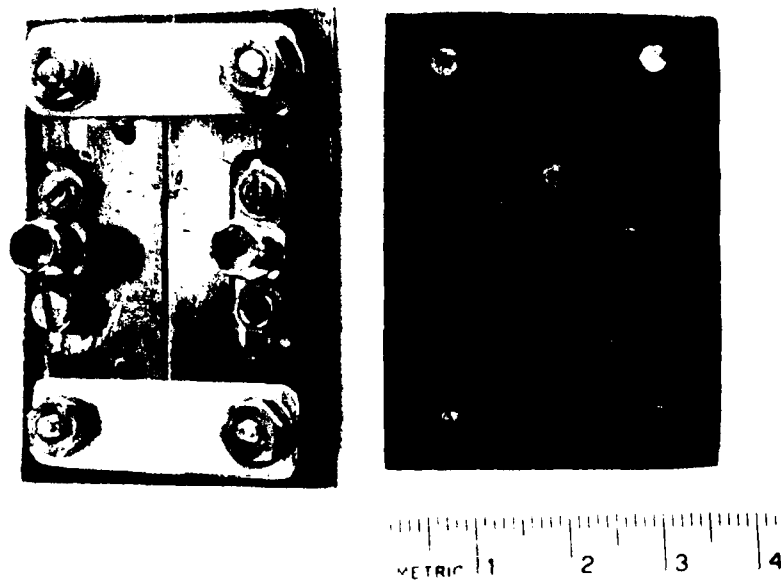


FIGURE 2.1 FRONT AND REAR VIEW OF .2 X 12.6 MM SERIAL MICROSTRIP SLOT TEST BOARD

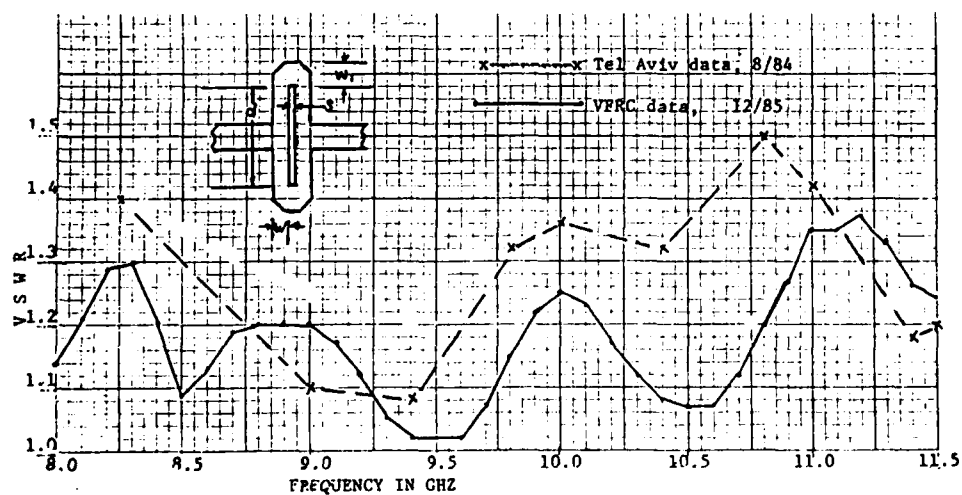


FIGURE 2.2. COMPARISON OF SINGLE X-BAND SLOT VSWR MEASUREMENTS AT TEL-AVIV UNIVERSITY AND AT VPRC. DIMENSIONS (in mm) $d = 12.1$, $w = .45$, $w_1 = .90$, $S = .1$, $h = .79$, $\epsilon_r = 2.2$.

Mitering slot ends and microstrip line ends at each connector made small reductions in VSWR and these changes were incorporated. The resulting impedance performance of a .2 mm x 12.1 mm slot on a 5.4" run is shown in Figure 2.2; the VFRC test data compares favorably with the Tel-Aviv University data also illustrated.

2.2 DIELECTRIC LAYER TRUNCATION EFFECTS

Dielectric-coated conductors, as noted in [7] and discussed in Section 3, can support a non-radiating hybrid mode which radiates at a dielectric truncation. Figure 2.3 shows an example of this effect: the radiation pattern of a single .2 mm slot in the center of a 15.25 cm board having both metal ground plane and dielectric sheet ending at ± 7.63 cm from the slot. The multilobed pattern results from the reradiation at the board ends which are 4.32 wavelengths apart at 8.5 GHz, the test frequency.

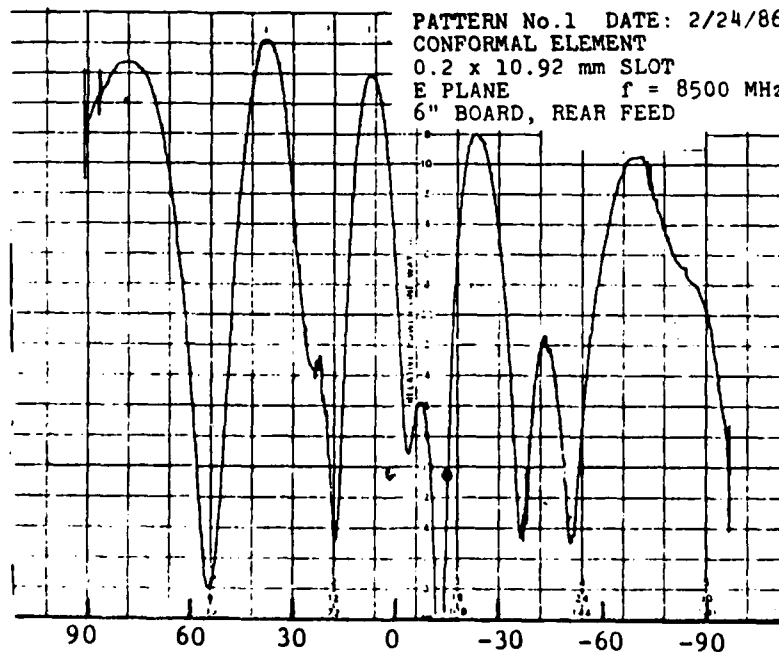


FIGURE 2.3 ANTENNA PATTERN OF .5 X 12.6 MM MICROSLLOT ON 15.3 CM DIELECTRIC SUBSTRATE. $\epsilon_r = 2.2$, CONNECTORS BEHIND GROUND PLANE.

In Figure 2.3, there are two predominant cyclic pattern systems, one having a 22 degree period and the other a 14 degree period. The separation of pattern nulls should be related to $\sin^{-1} \lambda/L$, where L is the separation of radiators in the two-radiator system.

It is interesting to try the spillover radiation hypothesis of Section 3 on this system, considering L as 2.16λ , half the board length, and assuming the 50 ohm line velocity of 1.37 times free space velocity. Then

$$\Delta\phi = 1.37 (2.16\lambda) \sin 22 \text{ deg.} = 399 \text{ deg.}$$

Since $\Delta\phi$ is by definition 360 deg., a velocity error of $(1 - 399/360) = 10.9\%$ is indicated by the computation. To force the 360 deg. result, a reduction of $\sqrt{\epsilon_e}$ from 1.37 to 1.236 is required. Thus, a spillover current-generated hybrid mode with a velocity 10.9% lower than the 50 ohm microstrip velocity is indicated.

Testing then continued on the 35.6 x 50.8 mm board with the .5 mm x 12.6 mm shunt slot sketched in Figure 1.1. The slot radiation pattern shown dotted in Figure 2.4 has a theoretical slot's beamwidth of 55 deg., but shows deviations at the -15 dB level, indicating the possible presence of radiation from dielectric truncations.

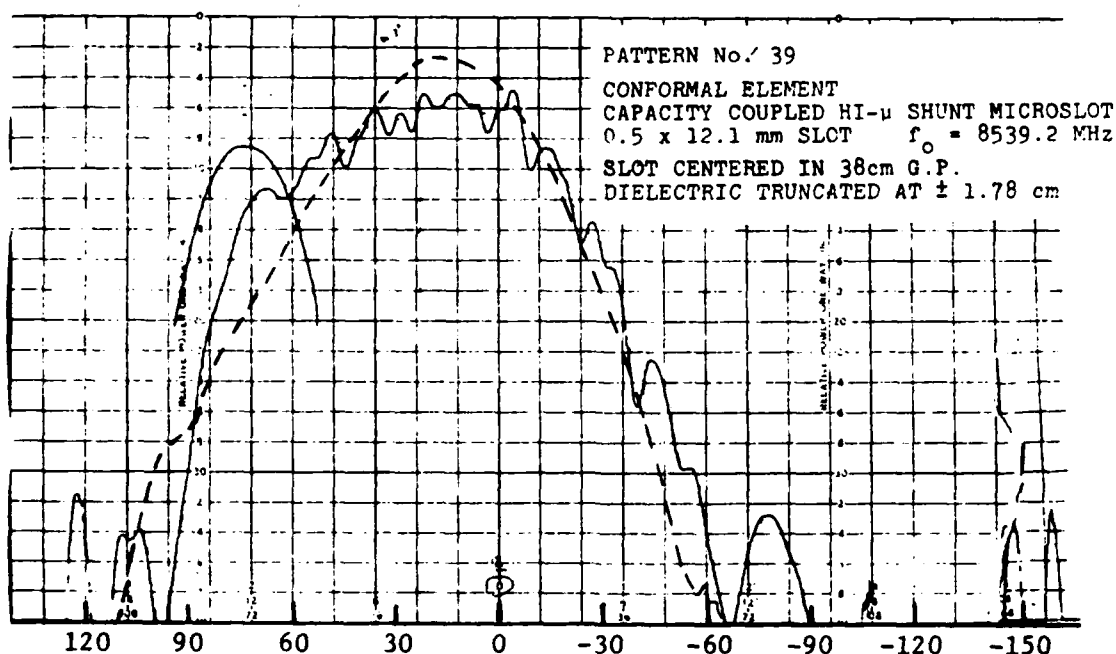


FIGURE 2.4. ANTENNA PATTERN: COMPARISON OF PATTERNS OF .5 X 12.6 MM SLOT RADIATOR WITH (SOLID LINE) AND WITHOUT 38 CM X 20 CM GROUND PLANE

The solid trace is the same radiator set in a 38 cm long by 20 m wide ground plane: the metal edges are now spaced 38 cm while the dielectric sheet width remains at 3.56 cm. The metal sheet edge effects are clearly indicated by a fine ripple relating to the 10.8 wavelength separation of the metal edges. The overall pattern distortion remains present in the radiation pattern, however, indicating the probability of dielectric truncation radiation effects.

Two possible sources of excitation of hybrid modes are apparent:

- the spillover currents carried on the top of the 50 ohm feedlines as discussed in Section 3.

- radiation from the microstrip open circuit at the junction of the microstrip-to-coaxial line adapter.

As described above, it is possible that spillover currents on the 6.85 cm feedlines are significant radiation source in the 15.25 cm board pattern shown in Figure 2.2. On the short runs of the 3.56 cm board patterns shown in Figure 2.3, however, it is possible that the microstrip open circuit of the microstrip-coax adapter is the major contribution to hybrid mode excitation/dielectric truncation radiation. This possibility is also discussed in connection with the serial slot patterns of the next section.

2.3 SERIES SLOT PATTERN

One goal of this study has been to determine the microslot antenna's useful bandwidth as a radiator. The final unit tested shown in Figure 2.1 was freeest from extraneous radiation effects and was measured over the 8.0 to 11.0 frequency band to permit that measurement. Its VSWR is given in Figure 2.5.

The vee-slot antenna was also tested because it had achieved higher gain than the slot in the shunt radiator version. It had lower measured gain than the .5 mm slot radiator, which confirmed the validity of Dr. Kisliuk's analysis of the microstrip slot as a coupled line system, a feature not present in the vee-slot design. Its pattern at 9 GHz is shown in Figure 2.9.

Antenna patterns were taken from 8 to 11 GHz; typical patterns for the .5 x 12.6 mm slot are shown in Figs. 2.6 - 2.8 and summarized in the graphs of Figure 2.10. At 8 GHz, the pattern beamwidth is slightly greater than theoretical (58 deg. vs. 56 deg. theoretical), has good pattern symmetry to a -15 dB level, and shows little beam tilt. The 9 GHz pattern shows a shoulder developing near + 90 deg., a lobe developing at -90 deg. and a

change of sign of the beam tilt. In the 10.5 GHz pattern, the energy at -90 deg. has reached -7.5 dB with a definite null appearing at +23 deg. right.

The pattern beam tilt appears related to the substrate board width: at the zero beam tilt frequency of 8.4 GHz seen in Figure 2.10b, the substrate is exactly 1.0 wavelengths wide. The pattern null, however, appears related to radiation from the microstrip open circuit at the input microstrip/coax adapter. Consider that the substrate edge and the microslot act as a two radiator set: at 10.5 GHz, computation of path lengths shows that these two sources are 180 deg. out of phase when viewed at -23 deg., the angle of the pattern null. The fact that this effect occurs only on the input connector side of the pattern indicates that only input connector radiation is involved in distorting the pattern.

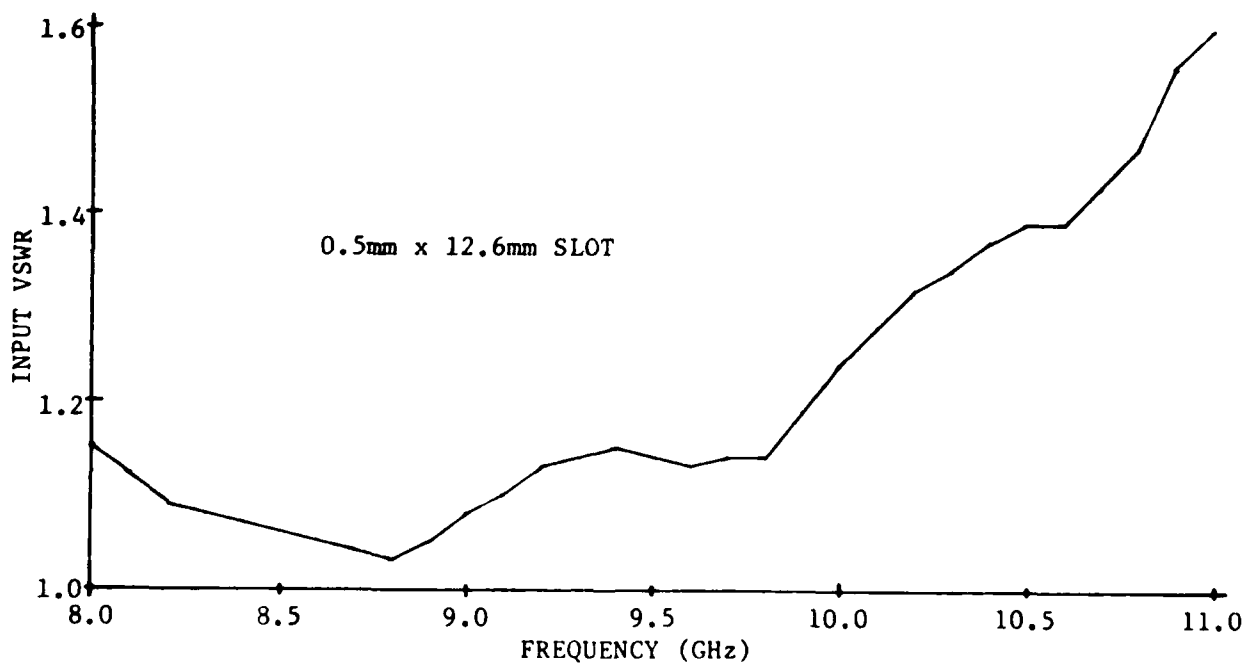


FIGURE 2.5. VSWR OF .5 X 12.6 MM SLOT RADIATOR USED IN PATTERN TESTS.

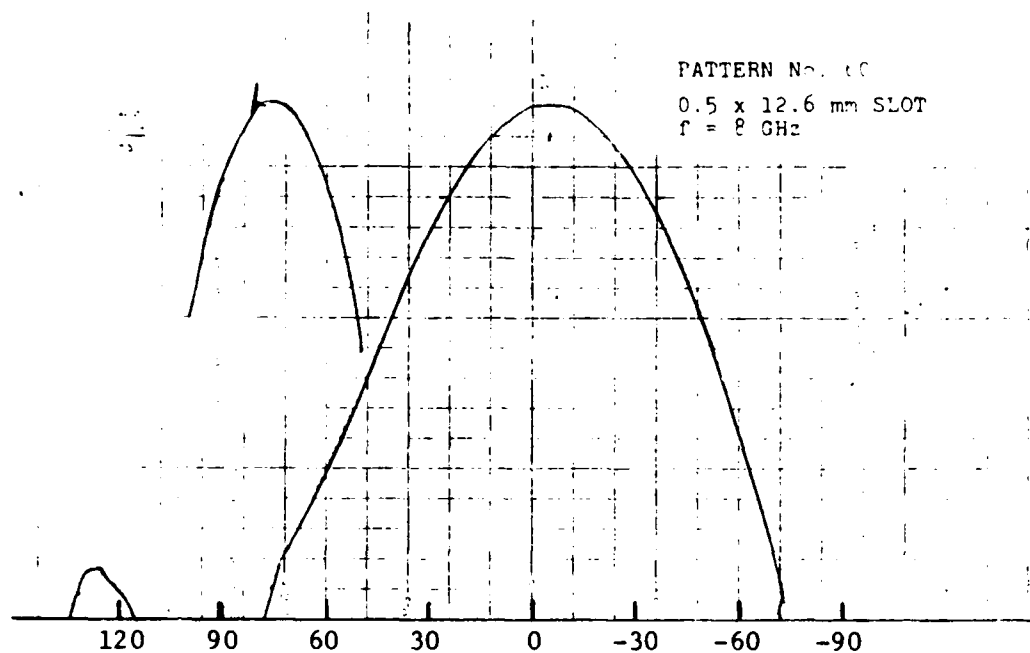


FIGURE 2.6. ANTENNA PATTERN: .5 x 12.6 mm SLOT AT 8.0 GHz

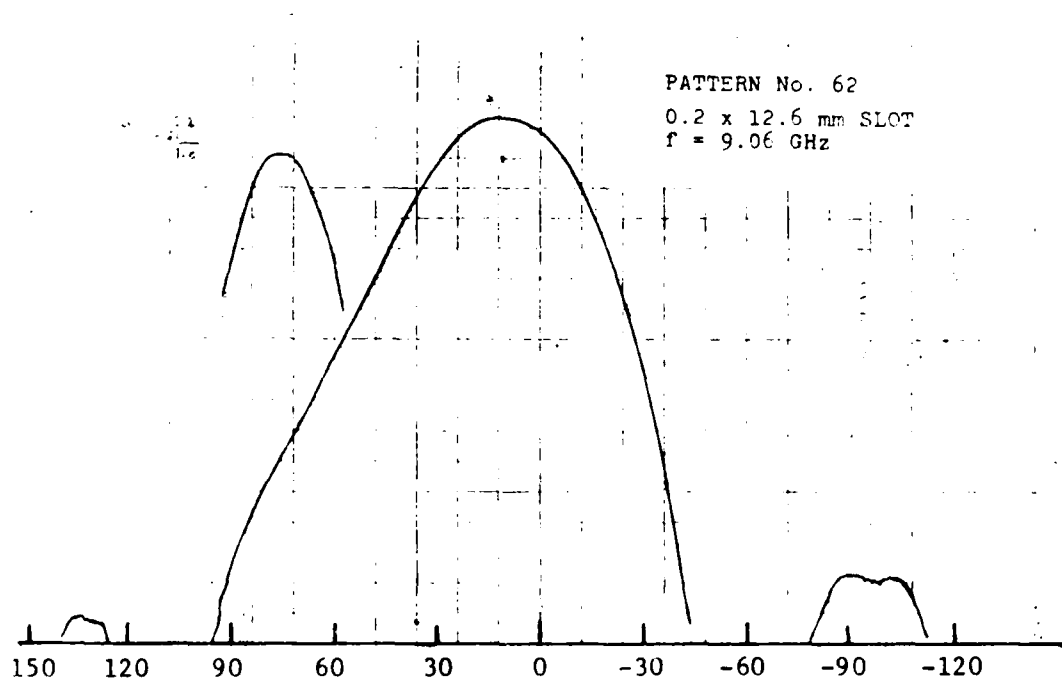


FIGURE 2.7. ANTENNA PATTERN: 5 X 12.6 MM SLOT AT 9.0 GHz

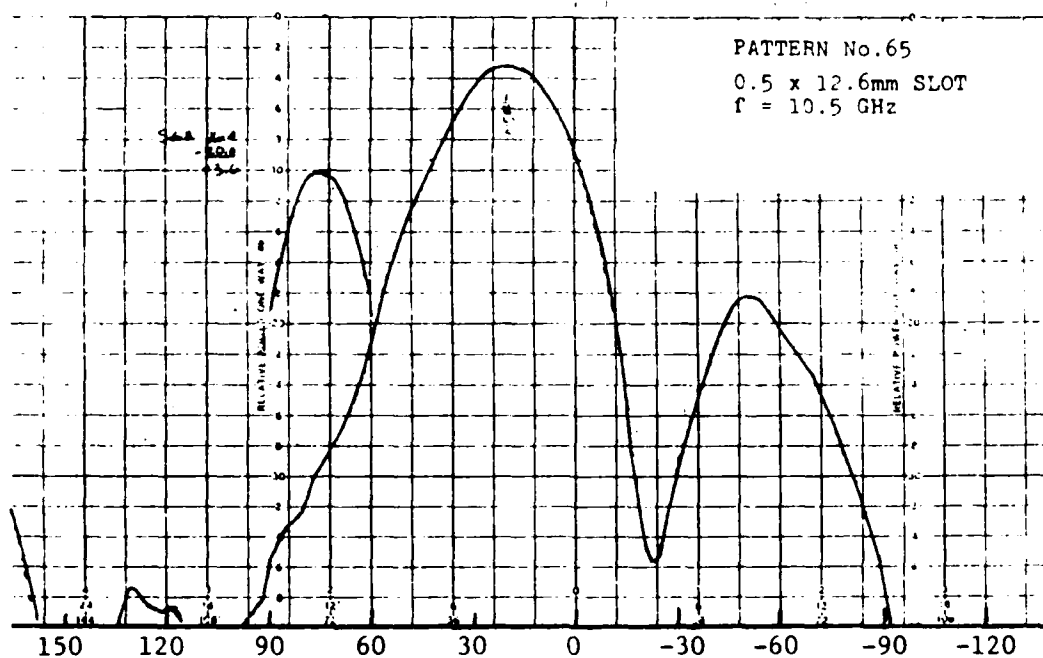


FIGURE 2.8. ANTENNA PATTERN: .5 X 12.6 MM SLOT AT 10.5 GHz.

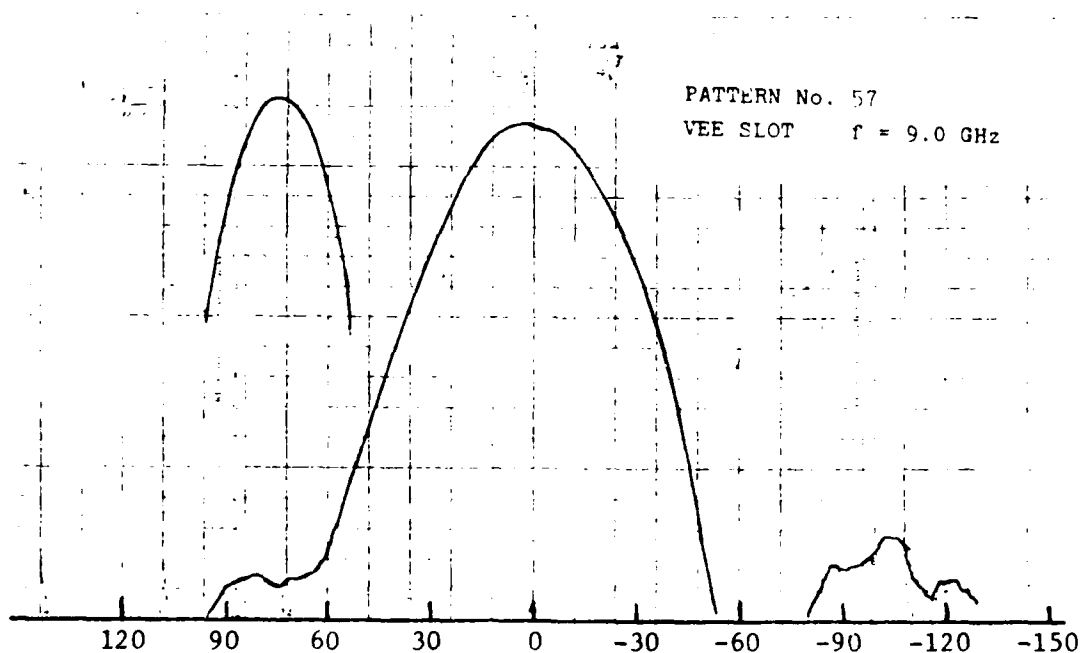


FIGURE 2.9. ANTENNA PATTERN; .5 MM VEE SLOT ANTENNA AT 9.0 GHz.

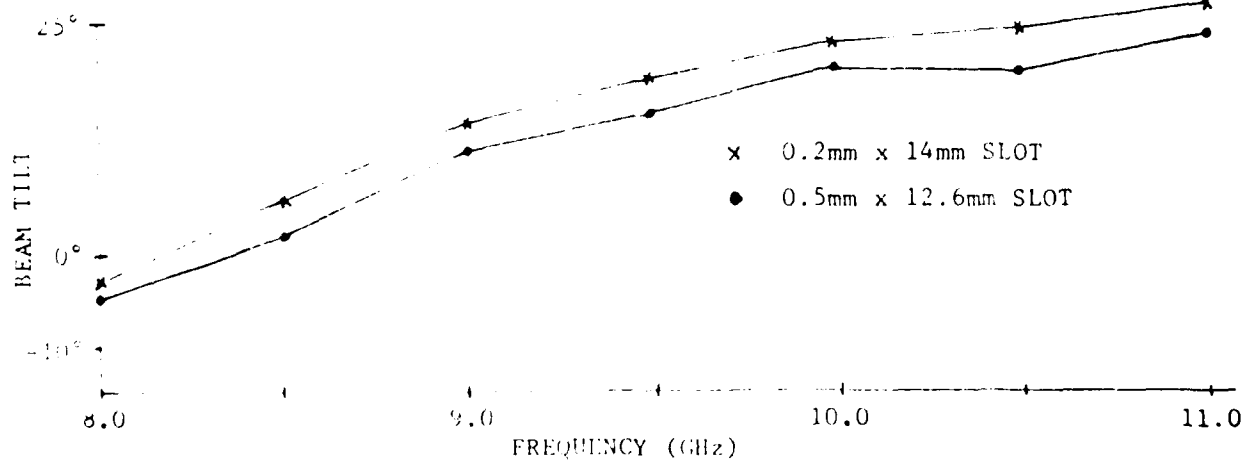
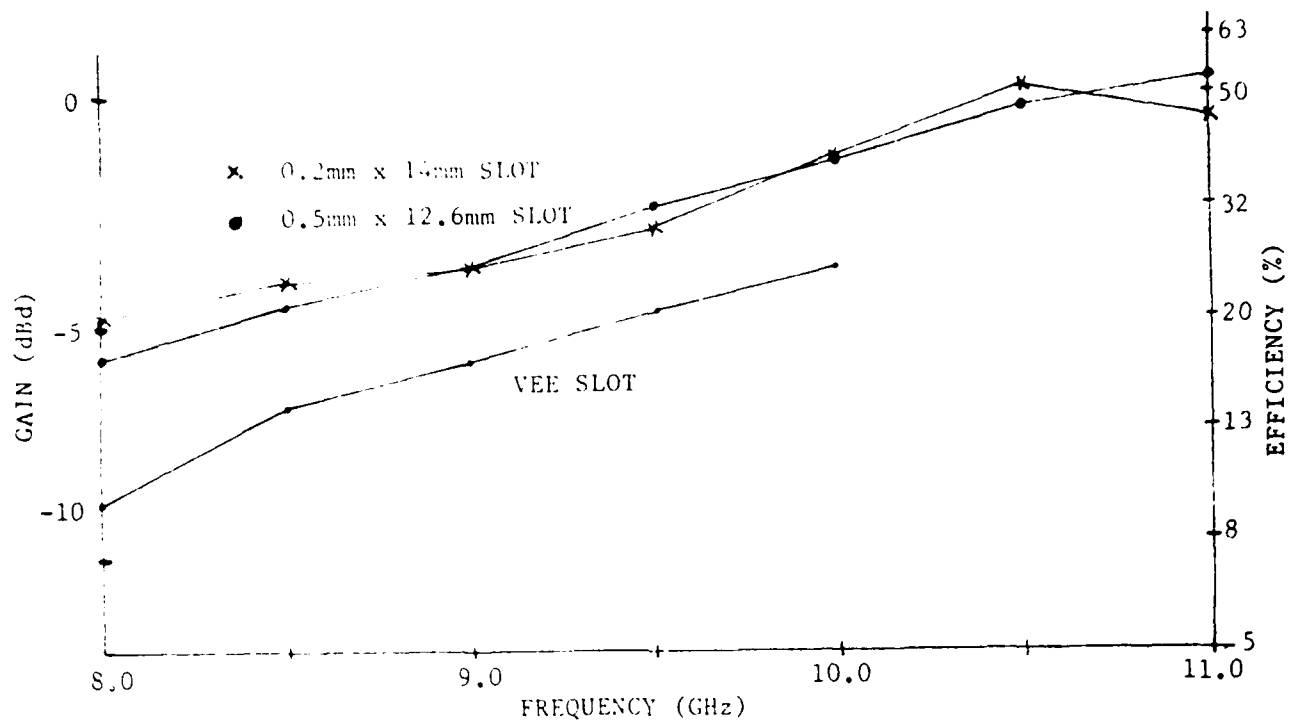


FIGURE 2.10. GAIN AND BEAM TILT VS FREQUENCY GRAPHS FOR .5 X 12.6 MM AND .2 X 14 MM MICROSTRIP SLOT AND .5 MM VEE SLOT RADIATORS.

2.4 GAIN AND EFFICIENCY

The antenna gains measured in this study are referred to the gain of a half-wave dipole for testing convenience. To relate to the average power radiated a fictitious isotropic radiator is defined which has uniform radiation over a spherical shell surrounding the antenna. The dipole gain relative to an isotrope is given in Reference 13 and other places as 1.64 or + 2.15 dB. One should also note that all measured gains include dielectric and $I^2 R$ losses in the antenna. Directivity also relates to main beam peak power relative to an isotropic source, but excludes any $I^2 R$ or dielectric losses. Directivity, therefore, can be defined analytically without involving the specific antenna material or other considerations.

Efficiency must be defined relative to the theoretical gain or directivity of the antenna type chosen, e.g., the slot radiating into a half space defined by the infinite ground plane containing the slot. The theoretical gain into a half space is + 3 dB above a dipole or + 5.15 dB above an isotrope. An efficiency scale calculated on this basis is shown in the right-hand ordinate of Figure 2.10's gain slot.

The patterns in the 8.0 - 9.0 GHz region are relatively undistorted by the reradiation from the dielectric truncation as evidenced both by pattern symmetry and absence of endfire lobe at -90 deg., and the efficiency shown in this region (20-25%) relates closely to the values measured and reported in the First Interim Report.

The values of gain above 9 GHz are suspect because of distortion from truncation radiation. This increased radiation, it is noted, correlates

with the increased input reflection coefficient: it is expected that improved connector match would eliminate the end-fire radiation and improve the gain correlation with the lower frequency readings.

3. RADIATION OF MICROSTRIP MEANDER-LINE SLOT ANTENNA

The microstrip meander line (Franklin) antenna was introduced in 1953 by Fubini [1]. Later investigations of the Franklin microstrip antenna (and array) were reported by Solbach [2] and Kisliuk [3]. Explicit expressions for input impedance and radiation efficiency of a single microstrip meander-line slot antenna were derived by Kisliuk [4]. Radiation patterns of single slot antennas and antenna arrays were reported in [2], [4] and [5]. It was observed in [4] that the electromagnetic radiation of microstrip meander-line slot antennas is generated by the voltage distribution on the slot (magnetic current), and by the fractional currents flowing on the upper surface of the straight microstrips [6] feeding the meander line (see Figure 3.1). Hybrid surface waves excited on both sides of the feeding microstrips [7] generate radiation (space) waves at the input and output truncations of the microstrip dielectric board ($z = z_1$) and $z = z_2$); radiation generated by surface waves at the truncation of the dielectric board has been reported in [8].

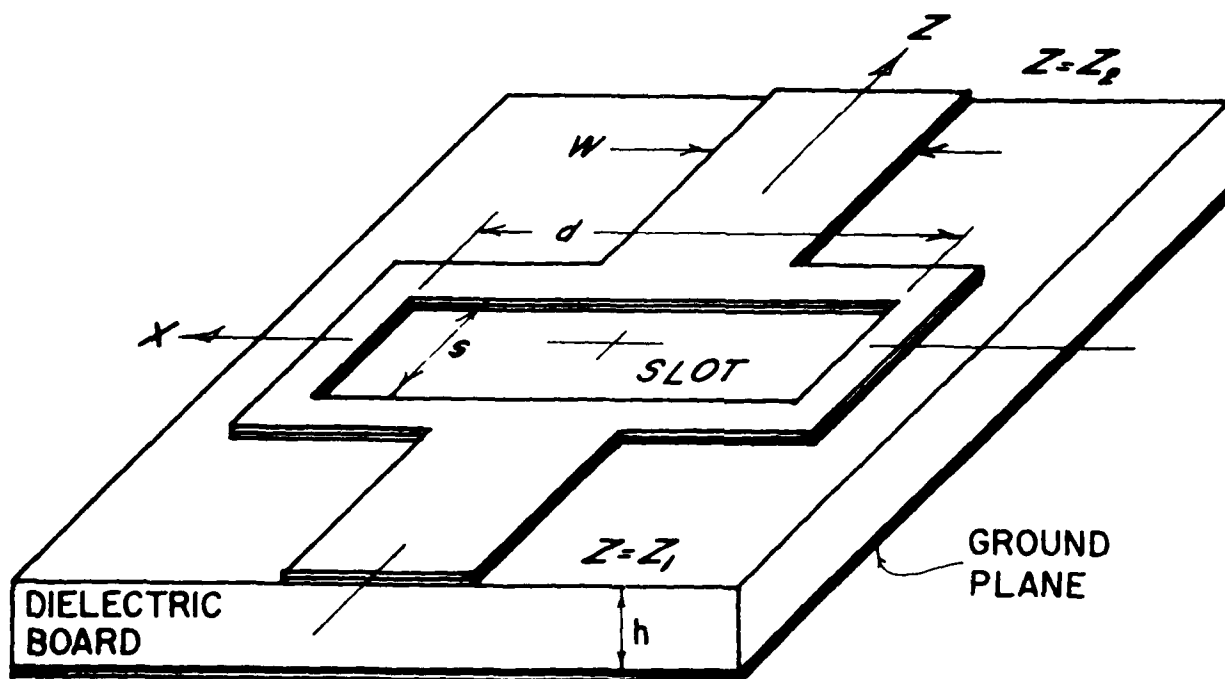


FIGURE 3.1. THE MICROSTRIP MEANDER-LINE SLOT ANTENNA

This section presents a detailed derivation of the radiation-zone electric fields generated by the slot, by the spillover currents, and by the hybrid surface waves at the truncations of the dielectric board on which the slot antenna has been etched.

3.1 FIELDS IN A SPHERICAL COORDINATE SYSTEM

The computation of the field components in the radiation (far-field) zone requires the introduction of spherical coordinates with the polar axis in the x direction, as shown in Figure 3.2; the Cartesian coordinates in Figure 3.2 are the same as in Figure 3.1. The transition from Cartesian unit vectors to the spherical ones are given by the following formulas:

$$\hat{x} = \hat{r}\cos\theta - \hat{\theta}\sin\theta, \quad (3.1a)$$

$$\hat{y} = \hat{r}\sin\theta\cos\phi + \hat{\theta}\cos\theta\cos\phi - \hat{\phi}\sin\phi, \quad (3.1b)$$

$$\hat{z} = \hat{r}\sin\theta\sin\phi + \hat{\theta}\cos\theta\sin\phi + \hat{\phi}\cos\phi. \quad (3.1c)$$

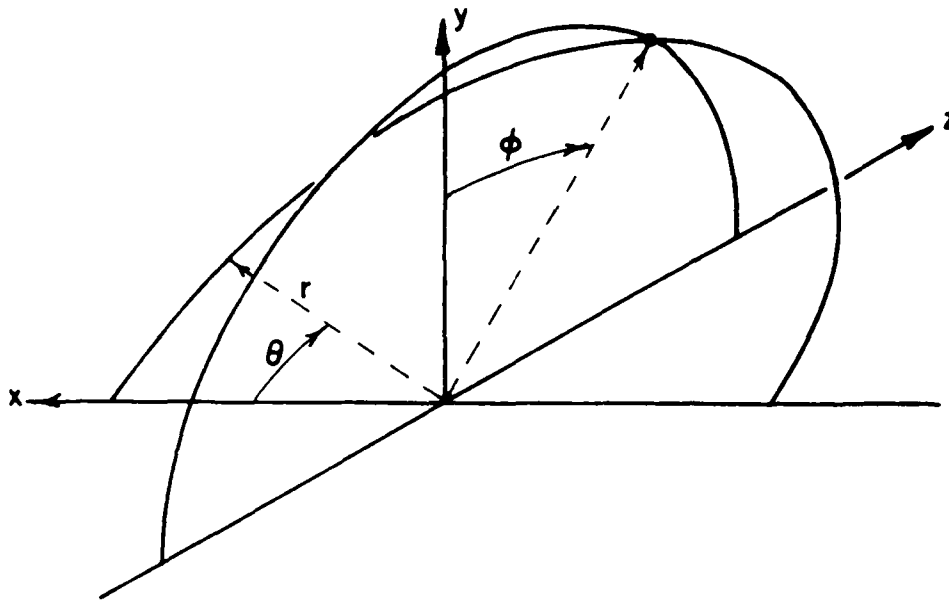


FIGURE 3.2. SPHERICAL COORDINATES IN THE FAR-FIELD ZON

In the region above the microstrip where $y > 0$, the range of the polar angle θ is from 0 to π , and the range of the azimuthal angle ϕ is from $-\pi/2$ to $\pi/2$. The vector potential functions generated by electric and magnetic currents are [9]:

$$\bar{A} = \frac{\mu_0}{4\pi} \int_V \bar{J}_e \exp(-jkR) \frac{1}{R} dx_0 dy_0 dz_0, \quad (3.2)$$

$$\bar{A}^* = \frac{\epsilon_0}{4\pi} \int_V \bar{J}_m \exp(-jkR) \frac{1}{R} dx_0 dy_0 dz_0, \quad (3.3)$$

where \vec{J}_e and \vec{J}_m are the vector densities of the electric and magnetic currents, respectively,

$$R = [(x-x_0)^2 + (y-y_0)^2 + (z-z_0)^2]^{0.5}, \quad (3.4)$$

and $k = \omega/\epsilon_0\mu_0$. x, y, z are the coordinates of the observation (field) point, x_0, y_0, z_0 are the coordinates of the source point.

When the distance r from the observation point to the coordinate origin (Figure 3.1) is very large compared to the dimensions of the radiating body, the following standard approximations are used: $R \approx r - x_0 \cos\theta - y_0 \sin\theta \cos\phi - z_0 \sin\theta \sin\phi$, and the integrals (2) and (3) are simplified.

$$\vec{A} = \frac{\mu_0 \exp(-jkr)}{4\pi r} \int_V \vec{J}_e \exp(j\psi) dx_0 dy_0 dz_0, \quad (3.5)$$

$$\vec{A}^* = \frac{\epsilon_0 \exp(-jkr)}{4\pi r} \int_V \vec{J}_m \exp(j\psi) dx_0 dy_0 dz_0, \quad (3.6)$$

where

$$\psi = \beta_1 x_0 + \beta_2 z_0 + \beta_3 y_0, \quad (3.7a)$$

$$\beta_1 = k \cos\theta, \quad (3.7b)$$

$$\beta_2 = k \sin\theta \sin\phi, \quad (3.7c)$$

$$\beta_3 = k \sin\theta \cos\phi \quad (3.7d)$$

The angular components of the potential functions (5) and (6) are obtained from (3.1)

$$A_\theta = -A_x \sin\theta + A_y \cos\theta \cos\phi + A_z \cos\theta \sin\phi, \quad (3.8a)$$

$$A_\phi = -A_y \sin\phi + A_z \cos\phi. \quad (3.8b)$$

The angular (transverse) components of the electric field in the far-field (radiation) zone are obtained from (8) utilizing the basic equation for the vector potential functions:

$$\vec{E} = -\frac{1}{\epsilon_0} \nabla \times \vec{A}^* - j\omega \vec{A} - \nabla \phi,$$

where ϕ is the scalar potential function [9]. In the far-field zone $(\nabla \phi)_{tr} \approx 0$, and

$$\nabla \times \vec{A}^* \approx -\hat{\theta} \frac{\partial A_{\phi}^*}{\partial r} + \hat{\phi} \frac{\partial A_{\theta}^*}{\partial r} \approx jk(\hat{\theta} A_{\phi}^* - \hat{\phi} A_{\theta}^*).$$

Thus we obtain explicit expressions for the transverse components of the electric field in the radiation zone:

$$E_{\phi} = jk\left(\frac{1}{\epsilon_0} A_{\theta}^* - \frac{\eta}{\mu_0} A_{\phi}\right), \quad (3.9a)$$

$$E_{\theta} = jk\left(-\frac{1}{\epsilon_0} A_{\phi}^* - \frac{\eta}{\mu_0} A_{\theta}\right). \quad (3.9b)$$

3.2 RADIATION FROM THE SLOT

The voltage across the slot is

$$V_{\text{slot}} = 2V_o, \quad (3.10)$$

where V_o is the voltage of the odd mode in the meander line enveloping the slot [4].

It has been shown in [4] that if the width of the meander line is less than the thickness of the dielectric board (Figure 3.1), the influence of the right-angle bends at the ends of the slot, as well as the influence of the T-junctions at the input and output of the slot radiator, can be neglected. Simplified expressions for such a meander-line radiating slot are derived in Reference 12. As shown in Reference 12, equation (10), above, yields

$$V_{\text{slot}} = V_s \frac{\sinh[\gamma_o(d/2 - |x|)]}{\sinh(\gamma_o d/2)}, \quad (3.11)$$

where

$$V_s = 2V_{inc} \frac{1+p}{1+S/\tanh(\gamma_o d/2)} \quad (3.12)$$

is the voltage at the center of the slot, V_{inc} is the voltage wave incident upon the input (Figure 3.3) of the meander line, and p is the reflection coefficient from the input of the meander line radiating slot (Figure 3.3). Explicit expressions for S and p from Reference 12 are:

$$V_e = V_o \frac{\cosh \theta_o}{\cosh \theta_e} S, \quad p = \frac{Z_{in} - Z_c}{Z_{in} + Z_c},$$

$$S = \frac{2Y_o Z_L + \tanh \theta_o}{2Y_e Z_L \tanh \theta_e + 1}.$$

The equivalent magnetic current density of the slot is

$$\vec{J}_m = -\hat{x} 2 \frac{V_{slot}}{s} \delta(y) \quad (3.13)$$

where s is the width of the slot, and the factor 2 accounts for the influence of the conductive plane surrounding the slot. The substitution of (3.13) into (3.6) yields

$$\vec{A}^* = -\hat{x} \frac{\epsilon_o}{2\pi} V_s D \frac{\exp(-jkr)}{r} \quad (3.14)$$

where

$$D = \frac{1}{s} \int_{-s/2}^{s/2} \exp(j\beta_2 z) dz \int_{-d/2}^{d/2} \frac{\sinh[\gamma_o(d/2 - |x|)]}{\sinh(\gamma_o d/2)} \exp(j\beta_1 x) dx. \quad (3.15)$$

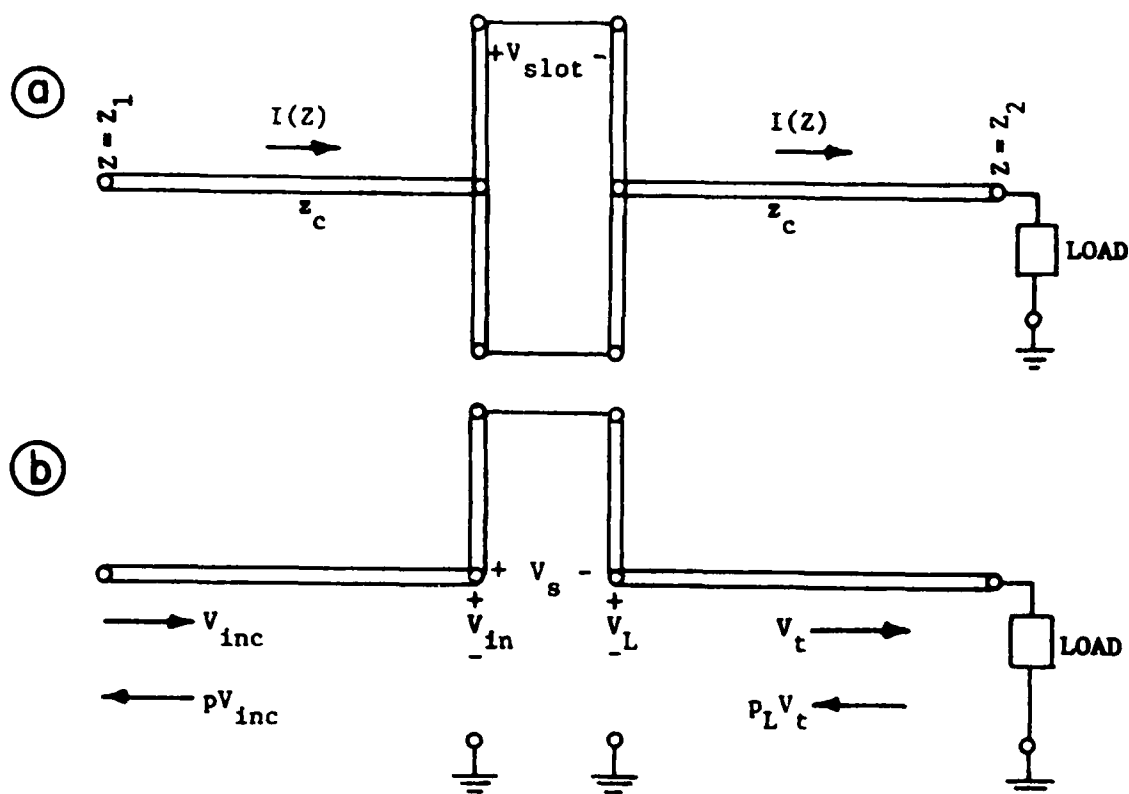


FIGURE 3.3. SIMPLIFIED EQUIVALENT CIRCUIT OF A MICROSTRIP MEANDER-LINE SLOT ANTENNA

- a. With full meander line
b. With folded meander line

The integrals in (15) are readily obtained:

$$D = \frac{2\gamma_o [\cosh(\gamma_o d/2) - \cos(\beta_1 d/2)]}{(\gamma_o^2 + \beta_1^2) \sinh(\gamma_o d/2)} \text{sinc}(\beta_2 s/2), \quad (3.16)$$

where

$$\text{sinc}(x) = \frac{\sin x}{x}. \quad (3.17)$$

The angular components of the vector potential function (14) are found from (8):

$$A_\theta^* = \frac{\epsilon_o}{2\pi} V_s D \sin\theta \frac{\exp(-jkr)}{r}, \quad (3.18a)$$

$$A_\phi^* = 0. \quad (3.18b)$$

Equations (3.9) and (3.18) yield the angular (transverse) components of the electric field generated by the slot in the far field zone:

$$E_{\phi}^{\text{slot}} = j \frac{k}{2\pi} V_s D \sin\theta \frac{\exp(-jkr)}{r}, \quad (3.19a)$$

$$E_{\theta}^{\text{slot}} = 0. \quad (3.19b)$$

3.3 RADIATION FROM SPILLOVER CURRENTS

The fractional currents that flow on top of the microstrips [6] are called spillover currents. The back currents flow on the ground plane in the region $|x| > w/2$ (Figure 3.1) and can be replaced by an image strip, carrying the same spillover current in the opposite direction, and placed at a distance $2h$ from the real strip; it is assumed that the space between the real strip and the image strip ($0 \leq y \leq 2h$) is filled with the dielectric material of the dielectric board.

If the distribution of the spillover currents across the top of the microstrip (x-direction, Figure 3.1) is assumed uniform, the current density vector of the spillover currents is given by

$$\vec{J}_e = \hat{z} \frac{I_s(z)}{w} [\delta(y) - \delta(y+2h)], \quad (3.20)$$

where

$$I_s(z) = qI(z) \quad (3.21)$$

is the spillover current, $I(z)$ is the total current of the microstrip line, and q is a constant [6].

The current distribution on the straight microstrip lines feeding the meander-line slot radiator is found from the equivalent circuit shown in Figure 3.3.

$$I(z) = \begin{cases} \frac{V_{inc}}{Z_c} [\exp(-j\beta z) - p \exp(j\beta z)] & \text{for } z_1 \leq z \leq 0 \\ \frac{V_t}{Z_c} [\exp(-j\beta z) - p_L \exp(j\beta z)] & \text{for } 0 \leq z \leq z_2 \end{cases} \quad (3.22)$$

where V_{inc} is the voltage wave incident on the reference plane $z = -0$, p is the reflection coefficient at $z = -0$, V_t is the transmitted voltage wave at the output of the meander line slot radiator ($z = +0$), and p_L is the reflection coefficient of the "load" at the output terminals of the slot radiators (Figure 3.3); Z_c is the characteristic impedance of the feeding microstrip lines.

The substitution of (3.20), (3.21) and (3.22) into (3.5) yields

$$\bar{A} = \hat{z} \frac{\mu_c}{2\pi} q \frac{V_{inc}}{Z_c} C \frac{\exp(-jkr)}{r} \quad (3.23)$$

where

$$C = jR \sin(\beta_4 h) \text{sinc}(\beta_1 w/2) \exp(-j\beta_3 h), \quad (3.24)$$

$$\beta_4 = \sqrt{\epsilon_r} \beta_3, \quad (3.25)$$

$$R = R_1 + R_2 + R_3 + R_4, \quad (3.26a)$$

$$R_1 = \frac{1 - \exp[jz_1(\beta_2 - \beta)]}{j(\beta_2 - \beta)},$$

$$R_2 = -p \frac{1 - \exp[jz_1(\beta_2 + \beta)]}{j(\beta_2 + \beta)}, \quad (3.26b)$$

$$R_3 = \frac{V_L}{V_{inc}(1+p_L)} \frac{\exp[jz_2(\beta_2 - \beta)] - 1}{j(\beta_2 - \beta)}, \quad (3.26c)$$

$$R_4 = -p_L \frac{V_L}{V_{inc}(1+p_L)} \frac{\exp[jz_2(\beta_2 + \beta)] - 1}{j(\beta_2 + \beta)}, \quad (3.26d)$$

V_L is the output voltage of the meander-line slot radiator (see Figure 3.3).

The angular components of the potential function and of the radiation fields generated by the spillover currents are

$$A_\theta = qV_{inc} \frac{\mu_0}{2\pi Z_c} C \cos\theta \sin\phi \frac{\exp(-jkr)}{r}, \quad (3.27a)$$

$$A_\theta = qV_{inc} \frac{\mu_0}{2\pi Z_c} C \cos\phi \frac{\exp(-jkr)}{r}, \quad (3.27b)$$

$$E_\phi^{curr} = -jV_{inc} qk \frac{\eta}{2\pi Z_c} C \cos\phi \frac{\exp(-jkr)}{r}, \quad (3.28)$$

$$E_\theta^{curr} = -jV_{inc} qk \frac{\eta}{2\pi Z_c} C \cos\theta \sin\phi \frac{\exp(-jkr)}{r}. \quad (3.29)$$

For a standard 50Ω microstrip line ($Z_c = 50\Omega$) the impedance ratio in (3.28) and (3.29) is

$$\frac{\eta}{2\pi Z_c} = \frac{120\pi}{100\pi} = 1.2 \quad (3.30)$$

3.4 RADIATION FROM THE HYBRID SURFACE WAVE AT THE TRUNCATIONS OF THE DIELECTRIC

The microstrip quasi-TEM mode in a microstrip line generates a hybrid surface wave [7] that propagates along the microstrip with the phase velocity of the microstrip mode. It has been shown in [8] that the truncations of the dielectric are sources of radiation generated by a surface wave. The electric and magnetic fields of the hybrid surface wave that are tangential to the truncation planes $z = z_1$ and $z = z_2$ (Figure 3.1) are

$$\vec{E} = \hat{x}E_x + \hat{y}E_y, \quad (3.31a)$$

$$\vec{H} = \hat{x}H_x + \hat{y}H_y. \quad (3.31b)$$

On the input truncation plane $z = z_1$ the outward unit normal is $\hat{n}_1 = -\hat{z}_1$,

hence the equivalent current densities are

$$\vec{J}_{e1} = (\hat{x}H_{y1} - \hat{y}H_{x1})\delta(z-z_1), \quad (3.32)$$

$$\vec{J}_{m1} = (-\hat{x}E_{y1} + \hat{y}E_{x1})\delta(z-z_1). \quad (3.33)$$

On the output truncation plane $z = z_2$ the outward unit normal is $\hat{n}_2 = \hat{z}_2$,

and the equivalent current densities are

$$\vec{J}_{e2} = (-\hat{x}H_{y2} + \hat{y}H_{x2})\delta(z-z_2), \quad (3.34)$$

$$\vec{J}_{m2} = (\hat{x}E_{y2} - \hat{y}E_{x2})\delta(z-z_2). \quad (3.35)$$

It has been shown in [7] that the field components of a hybrid surface wave are

$$E_x = \begin{cases} E_{xi}f_3 & \text{for } y \leq h \\ E_{xe}f_4 & \text{for } y \geq h \end{cases} \quad (3.36a)$$

$$E_y = \begin{cases} E_{yi}f_1 & \text{for } y \leq h \\ E_{ye}f_2 & \text{for } y \geq h \end{cases} \quad (3.36b)$$

$$H_x = \begin{cases} H_{xi} f_1 / \eta & \text{for } y \leq h \\ H_{xe} f_2 / \eta & \text{for } y \geq h \end{cases} \quad (3.36c)$$

$$H_y = \begin{cases} H_{yi} f_3 / \eta & \text{for } y \leq h \\ H_{ye} f_4 / \eta & \text{for } y \geq h \end{cases} \quad (3.36d)$$

Explicit expressions for the computation of E_{xi} , etc. are given in

Reference 12. The functions f_i in (3.36) are:

$$f_1 = sV \cos(\xi y) \exp(-\alpha_x v + j\beta z), \quad (3.37a)$$

$$f_2 = sV \exp(-\alpha_x v - \alpha_y u + j\beta z), \quad (3.37b)$$

$$f_3 = sV \operatorname{sgn}(x) \sin(\xi y) \exp(-\alpha_x v + j\beta z), \quad (3.37c)$$

$$f_4 = sV \operatorname{sgn}(x) \exp(-\alpha_x v - \alpha_y u + j\beta z), \quad (3.37d)$$

$$u = y - n, \quad (3.38)$$

$$v = \begin{cases} x - w/2 & \text{for } x > w/2 \\ -x - w/2 & \text{for } x < -w/2 \end{cases} \quad (3.39)$$

$$\operatorname{sgn}(x) = \begin{cases} 1 & \text{for } x > w/2 \\ -1 & \text{for } x < -w/2 \end{cases} \quad (3.40)$$

V is the voltage of the microstrip quasi-TEM mode, and s is the excitation constant, which for a Duroid 5880 ($\epsilon_r = 2.2$) 50 Ω line is 0.01.

The substitution of (3.34)-(3.40) into the integrands of (3.5) and (3.6) yields

$$\vec{A} = \frac{\mu_0}{4\pi} V_{inc} \frac{s}{4\pi} Q_5 (\hat{x}Q_1 + \hat{y}Q_2) \frac{\exp(-jkr)}{r}, \quad (3.41)$$

$$\vec{A}^* = \epsilon_0 V_{inc} \frac{s}{4\pi} Q_6 (\hat{x}Q_3 + \hat{y}Q_4) \frac{\exp(-jkr)}{r}, \quad (3.42)$$

where Q_1-Q_6 are:

$$\begin{aligned} Q_1 &= -(H_{yi}P_4 + H_{ye}P_6)P_2, & Q_2 &= (H_{xi}P_3 + H_{xe}P_5)P_1, \\ Q_3 &= (E_{yi}P_3 + E_{ye}P_5)P_1, & Q_4 &= -(E_{xi}P_4 + E_{xe}P_6)P_2, \\ Q_5 &= Q_7 - Q_8, & Q_6 &= Q_7 + Q_8, \end{aligned}$$

The image components of the electric and magnetic currents in the region $y < 0$ due to the conductive ground plane (which is assumed infinite) are analytical continuations of the functions (3.37a) and (3.37c); the "cosine" components have an even image, while the "sine" components have an odd image. Thus, the hybrid wave radiation is generated mostly by the E_y and H_x components of the hybrid wave.

The transverse components of the radiation field generated by the hybrid surface wave due to the truncation of the dielectric are:

$$\vec{E}_{hybr} = jV_{inc} s \frac{k}{4\pi} [Q_6(Q_4 \cos\theta \cos\phi - Q_3 \sin\theta) + Q_2 Q_5 \sin\phi] \frac{\exp(-jkr)}{r} \quad (3.43)$$

$$E_{\theta}^{\text{hybr}} = jV_{\text{inc}} s \frac{k}{4\pi} [Q_5(Q_1 \sin\theta - Q_2 \cos\theta \cos\phi) + Q_4 Q_6 \sin\phi] \frac{\exp(-jkr)}{r} \quad (3.44)$$

The total radiation field is the sum of the fields derived above.

$$E_{\phi} = E_{\phi}^{\text{slot}} + E_{\phi}^{\text{curr}} + E_{\phi}^{\text{hybr}}, \quad (3.45)$$

$$E_{\theta} = E_{\theta}^{\text{curr}} + E_{\theta}^{\text{hybr}}. \quad (3.46)$$

The radial component of the pointing vector is

$$\Pi = (|E_{\phi}|^2 + |E_{\theta}|^2)/(240\pi), \quad (3.47)$$

and the total power radiated by the microstrip slot antenna which is

$$P_{\text{rad}} = \int_{-\pi/2}^{\pi/2} d\phi \int_0^{\pi} d\theta r^2 \Pi \sin\theta \quad (3.48)$$

can be found by numerical calculations, which will be reported later.

3.5 TAPERED MEANDER LINE SLOT ARRAY INVESTIGATIONS

Preliminary investigations of tapered meander-line slot arrays are reported in [10].

An array of 13 slots is shown in Figure 3.4; the width of slots is tapered leading to a taper in the amplitude of the voltage at the center of the slots. The widths of the slots are:

$$s_1 = s_{13} = 0.374 \text{ mm}$$

$$s_3 = s_{11} = 0.189 \text{ mm}$$

$$s_5 = s_9 = 0.116 \text{ mm}$$

$$s_2 = s_{12} = 0.282 \text{ mm}$$

$$s_4 = s_{10} = 0.141 \text{ mm}$$

$$s_6 = s_8 = 0.104 \text{ mm}$$

$$s_7 = 0.100 \text{ mm}$$

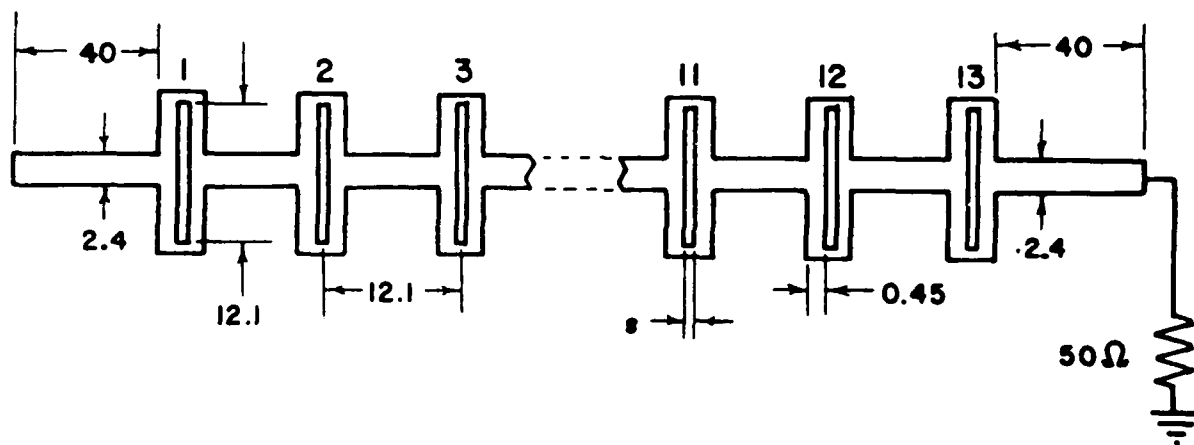


FIGURE 3.4. 13-SLOT ARRAY. THE WIDTH OF THE SLOTS IS TAPERED.

The radiation patterns of that array (Figure 3.4) are shown on Figure 3.5; the sidelobe level is about -15 dB.

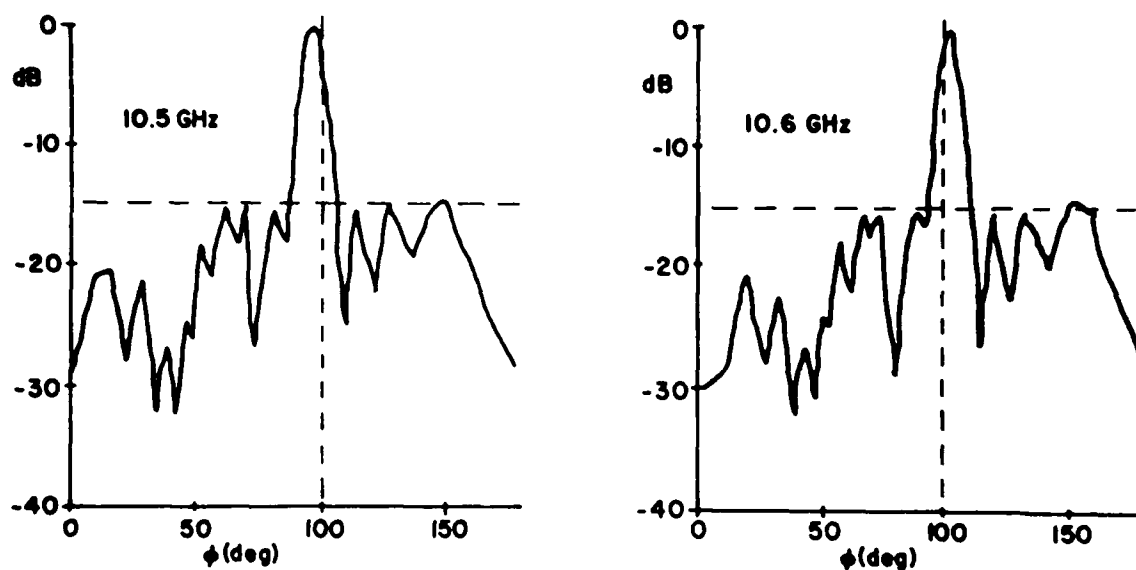


FIGURE 3.5. E-PLANE RADIATION PATTERNS OF THE SLOT ARRAY SHOWN IN FIG. 3.4.

Another array of 10 slots, where the width w of the straight microstrip lines feeding the slots is tapered, is shown in Figure 3.6. The design of this array is based on the relationship [2]

$$R_s(\Omega) = 45 \left(\frac{\lambda_0}{w} \right)^2 .$$

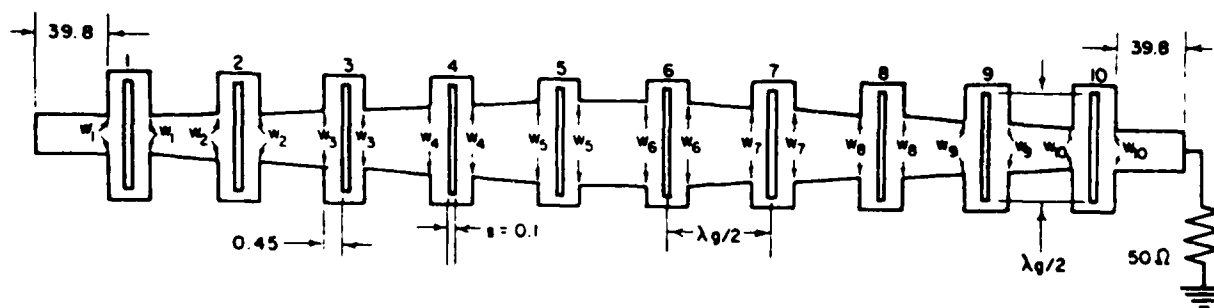


FIGURE 3.6. 10-SLOT ARRAY. THE WIDTH OF MICROSTRIP LINES FEEDING THE SLOTS IS TAPERED.

The radiation patterns of the 10-slot array in Figure 3.6 are shown in Figure 3.4; the sidelobe level is lower than -15 dB. The measured radiation efficiency of these arrays is above 75%.

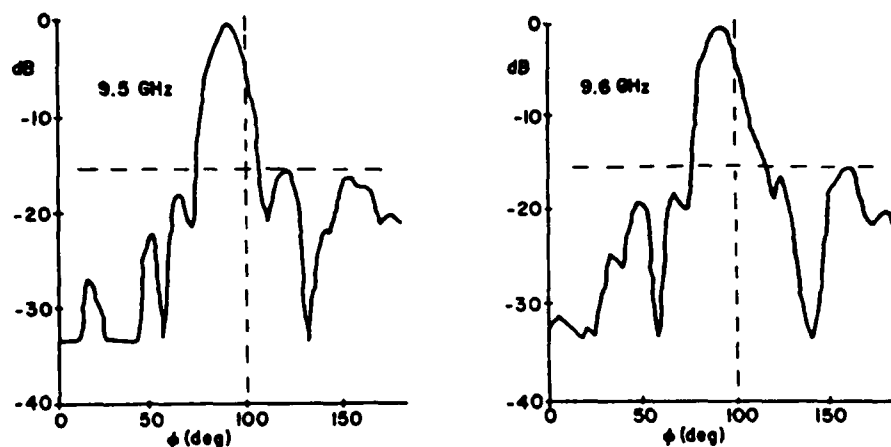


FIGURE 3.7. E-PLANE RADIATION PATTERNS OF THE SLOT ARRAY SHOWN IN FIG. 3.6.

4. CONCLUSIONS

The experimental and analytical studies described in this report detail information on two forms of microstrip slot radiator, the shunt form terminating a feedline and the serial form.

The shunt microslot radiator has a dipole pattern and exceeds 60% efficiency. It has a bandwidth determined by the stub line impedance and the substrate thickness and material. Its bandwidth in the present form is .6% and requires improvement before being a useful competitor for the patch antenna. The present microslot design compares unfavorably with the patch radiator in bandwidth.

The serial form of microslot radiator when measured with improved test methods exhibited dipole-like patterns when not distorted by radiation from dielectric truncations, and exhibited 20 to 25% efficiency. The pattern bandwidth exceeding 1 GHz was shown by patterns. Nonradiating hybrid modes can be generated by the microstrip launcher open circuit stub line as well

as by spillover currents on conductors. These modes transform to radiating modes at dielectric edge truncations. This radiation's magnitude is strongly correlated with input impedance match.

REFERENCES

- [1] E.G. Fubini, "Stripline Radiators," IRE Trans. Microwave Theory Techn., Vol. MTT-3, pp. 149-156, 1955.
- [2] K. Solbach, "Microstrip-Franklin Antenna," IEEE Trans. Antennas Propagat., Vol. AP-30, pp. 733-735, 1982.
- [3] M. Kisliuk, "The Conformal Microstrip Slot Antenna," 1983 Int. Symp. Antennas Propagat. Dig., Vol 1, pp. 166-169, Houston, Texas.
- [4] M. Kisliuk, "Microstrip-fed Radiating Slots and Slot Arrays," VFRC Quarterly Progress Report No. 45, pp. 46-58, Apr.-Sept. 1984.
- [5] W. Whistler, "Microstrip Slot Antenna - Experimental Investigation," VFRC Quarterly Progress Report No. 45, pp. 58-65, Apr.-Sept. 1984.
- [6] L. Lewin and T. Reuhle, "A Note on the Complex Pointing Vector and on the Fractional Current on the Upper Surface of a Microstrip Line," IEEE Trans. Antennas Propagat., Vol. AP-29, pp. 144-147, 1981.
- [7] M. Kisliuk and A. Axelrod, "Hybrid Surface Waves in Microstrip Lines," VFRC Quarterly Progress Report No. 47, pp. 69-75. Apr.-June 1985.
- [8] S.B.A. Fonseca and A.J. Giarola, "Microstrip Disk Antennas, Part 2: The Problem of Surface Wave Radiation by Dielectric Truncation," IEEE Trans. Antennas Propagat., Vol. AP-32, pp. 568-573, 1984.
- [9] C.A. Balanis, Antenna Theory: Analysis and Design, Harper & Row, Inc., New York, 1982.
- [10] G. Elazar, "Microstrip Slot Arrays," M.Sc. Thesis (in Hebrew), Tel-Aviv University, 1985. Adviser: Prof. M. Kisliuk.
- [11] Bailey and Deshpande, Integral Equation Formulation of Microstrip Antennas, IEEE Trans. Antennas & Propagat., Vol. AP-30, No. 4, July 1982, pp. 651-656.
- [12] M. Kisliuk and W. Whistler, Radiation of Microstrip Meander-Line Slot Antenna, VFRC Quarterly Progress Report No. 48, pp. 44-47, July-September 1986.
- [13] C.A. Balanis, Antenna Theory Analysis and Design, Harper & Row, 1982, pp. 124-126.

END

1-87

DTIC